JCB Journal of Cell Biology

ARTICLE

SUMOylation at the inner nuclear membrane facilitates nuclear envelope biogenesis during mitosis

Natasha O. Saik[1], Christopher Ptak[1], Saif Rehman[1], John D. Aitchison[1,2,3], Ben Montpetit[1,4], and Richard W. Wozniak[1]

As eukaryotic cells progress through cell division, the nuclear envelope (NE) membrane must expand to accommodate the formation of progeny nuclei. In *Saccharomyces cerevisiae*, closed mitosis allows visualization of NE biogenesis during mitosis. During this period, the SUMO E3 ligase Siz2 binds the inner nuclear membrane (INM) and initiates a wave of INM protein SUMOylation. Here, we show these events increase INM levels of phosphatidic acid (PA), an intermediate of phospholipid biogenesis, and are necessary for normal mitotic NE membrane expansion. The increase in INM PA is driven by the Siz2-mediated inhibition of the PA phosphatase Pah1. During mitosis, this results from the binding of Siz2 to the INM and dissociation of Spo7 and Nem1, a complex required for the activation of Pah1. As cells enter interphase, the process is then reversed by the deSUMOylase Ulp1. This work further establishes a central role for temporally controlled INM SUMOylation in coordinating processes, including membrane expansion, that regulate NE biogenesis during mitosis.

Introduction

The nuclear envelope (NE) is a double membrane structure that compartmentalizes the eukaryotic genome within the nucleus. The NE is composed of a cytoplasm facing outer nuclear membrane (ONM) that is continuous with the endoplasmic reticulum (ER) and a nucleoplasmic-facing inner nuclear membrane (INM). The INM functions as a platform that binds and organizes chromatin (Misteli, 2020; Ptak et al., 2014). During mitosis, chromatin is released from the INM and condenses as cells prepare for chromosome segregation. Once segregated, chromatin reassociates with the NE membranes of the newly forming daughter nuclei (Hetzer, 2010). The mitotic disassembly of the nucleus, including dissociation of chromatin–NE interactions, depends, in part, on the phosphorylation-dependent alterations in multiple protein–protein interactions, while reassembly is supported by dephosphorylation events (Hetzer, 2010) and SUMOylation (Moriuchi and Hirose, 2021; Moriuchi et al., 2016; Ptak et al., 2021). Coinciding with these mitotic posttranslational modifications and alterations in NE–chromatin interactions is the mitotic expansion of the NE membrane. In mammalian cells, where the NE is disassembled at the onset of mitosis, newly synthesized phospholipids are incorporated into the NE membranes that will reassociate with and enclose the segregated chromatin (Rodriguez Sawicki et al., 2019; Scaglia et al., 2014). In *Saccharomyces cerevisiae*, the NE does not break down during mitosis; rather, the NE membrane remains intact, undergoing visible and quantifiable expansion (Wang et al., 2016) as the duplicated genome is divided between mother and daughter cells. As in mammalian cells, mitotic expansion of the NE membrane in *S. cerevisiae* requires increased phospholipid synthesis (Campbell et al., 2006; Witkin et al., 2012).

A key intermediate in phospholipid synthesis and expansion of the NE membrane during mitosis is the lipid phosphatidic acid (PA; Kwiatek et al., 2020; Santos-Rosa et al., 2005), which is required for the de novo synthesis of glycerophospholipids. A key regulator of PA levels is a conserved family of proteins, termed lipins, that possesses phosphatidate phosphatase activity and functions to dephosphorylate PA to form diacylglycerol (DAG; Carman and Han, 2011; Han et al., 2006; Kwiatek et al., 2020; Lin and Carman, 1989; Péterfy et al., 2001). Lipins are in turn regulated by phosphorylation (Choi et al., 2011; Choi et al., 2012; Grimsey et al., 2008; Harris et al., 2007; Huffman et al., 2002; O'Hara et al., 2006; Peterson et al., 2011). For example, the *S. cerevisiae* lipin, Pah1, is phosphorylated at numerous sites by various kinases, including Cdk1 during mitosis. Phosphorylation of Pah1 inhibits its activity and appears to contribute to reducing its membrane association (Carman and Han, 2011)

[1]Department of Cell Biology, University of Alberta, Edmonton, Alberta, Canada; [2]Seattle Children's Research Institute, Seattle, WA, USA; [3]Department of Pediatrics and Department of Biochemistry, University of Washington, Seattle, WA, USA; [4]Department of Viticulture and Enology, University of California Davis, Davis, CA, USA.

Correspondence to Richard W. Wozniak: rick.wozniak@ualberta.ca.

and accessibility to PA. Activation of Pah1 is regulated solely by the NE/ER membrane-associated Nem1/Spo7 phosphatase complex, which binds to and dephosphorylates Pah1 (Karanasios et al., 2010; Santos-Rosa et al., 2005; Siniossoglou et al., 1998). How the binding of Pah1 to the Nem1/Spo7 phosphatase complex is regulated is not well understood. Consequences of the loss of Pah1 or either component of the Nem1/Spo7 complex include increased cellular PA levels, phospholipid production, and NE/ER membrane expansion (Campbell et al., 2006; Choi et al., 2011; Han et al., 2008; Han et al., 2006; Hassaninasab et al., 2017; Pascual et al., 2013; Santos-Rosa et al., 2005; Siniossoglou et al., 1998; Witkin et al., 2012). These observations, coupled with the observed increase in Cdk1-mediated phosphorylation of Pah1 during mitosis (Santos-Rosa et al., 2005), have led to the hypothesis that mitotic expansion of the NE membrane is facilitated by the inhibition of Pah1 activity. The molecular mechanism responsible for inhibiting the activity of Pah1 presumably involves its interactions with the Nem1/Spo7 complex; however, this has not been defined.

Expansion of the yeast NE membrane during mitosis occurs concomitantly with a recently described increase of SUMO conjugates that decorate the INM (Ptak et al., 2021). Protein SUMOylation often alters protein–protein interactions, either inhibiting associations or fostering interactions between SUMO-modified proteins and binding partners containing SUMO interaction motifs (Jentsch and Psakhye, 2013). During mitosis, Siz2, one of four yeast SUMO E3 ligases, binds the INM and catalyzes the addition of SUMO to specific proteins (Ptak et al., 2021). This process supports the reassociation of "heterochromatin-like" subtelomeric chromatin with the INM and activated genes with nuclear pore complexes as cells progress through mitosis (Ptak et al., 2021). Here, we show that SUMOylation events at the INM are required for the accumulation of PA at the INM and mitotic NE membrane expansion by inhibiting Pah1-Nem1/Spo7 complex formation. Together, our results establish temporally and spatially controlled SUMOylation as a mechanism for coordinating multiple mitotic events at the INM, including re-establishing NE–chromatin interactions and NE membrane expansion.

Results

NE binding of the SUMO E3 ligase Siz2 during mitosis supports membrane expansion

As yeast cells progress through mitosis, de novo lipid biogenesis produces additional NE membrane required for the formation of two nuclei (Campbell et al., 2006; Witkin et al., 2012). Coincident with NE membrane expansion, the SUMO E3 ligase Siz2 is phosphorylated and binds to the INM where it mediates SUMOylation of various INM-associated targets (Ptak et al., 2021). To determine whether these spatially and temporally regulated SUMOylation events play a role in mitotic NE membrane expansion, the surface area of the nucleus was determined at different cell cycle stages in asynchronously grown WT (*SIZ2*) cells and mutant cells producing a siz2^{S522A} point mutant that fails to bind the NE and SUMOylate NE targets during mitosis (see Ptak et al., 2021; Fig. S1 A). Cell morphology was used to define the cell cycle stage of individual cells, and the nuclear surface area was determined from a three-dimensional reconstruction of nuclei containing a diffuse nucleoplasmic reporter protein Pus1-GFP. The nuclear surface area of WT cells increased as cells progressed from G1- to M-phase (Fig. 1 A), consistent with previous reports (Wang et al., 2016). A comparison of WT and *siz2^{S522A}* mutant cells revealed similar nuclear surface areas in G1- and S-phase cells; however, *siz2^{S522A}* mutant cells had significantly reduced nuclear surface area in M-phase (Fig. 1 A).

The nuclear surface areas of WT and *siz2^{S522A}* cells were then measured as cells progressed through the cell cycle following release from α-factor–induced G1-phase arrest. Like cells in asynchronous cultures (Fig. 1 A), the synchronized population of WT and *siz2^{S522A}* cells initially exhibited similar nuclear surface areas and rates of increase through G1- and S-phase (0–60 min; Fig. 1 B). However, as cells progressed through mitosis (60–80 min), the nuclear surface area of WT cells continued to increase (coincident with increased Siz2-dependent SUMO conjugates at the INM; Fig. S1 A; Ptak et al., 2021), while in *siz2^{S522A}* cells, the nuclear surface area remained largely unchanged during mitosis. Following mitotic exit and formation of G1-phase progeny nuclei, the nuclear surface areas of WT and *siz2^{S522A}* cells decreased relative to mitotic nuclei, consistent with previous observations (Wang et al., 2016), and were again similar (Fig. 1 B).

It has been previously shown that cells arrested in metaphase continue phospholipid biogenesis, resulting in NE membrane expansion and distorted nuclear morphology (Campbell et al., 2006; Witkin et al., 2012; see Fig. 1 C and Fig. S1 B). These phenotypes are absent in mutants that inhibit phospholipid biogenesis (Witkin et al., 2012). Thus, the effect of the *siz2^{S522A}* mutant on NE membrane expansion during an M-phase arrest was tested. Cells were arrested in metaphase by the depletion of the anaphase-promoting complex subunit Cdc20. As shown in Fig. 1 C, depletion of Cdc20 for 2 h in an otherwise WT background resulted in large-budded, metaphase-arrested cells with extensive nuclear extensions. This was accompanied by the NE accumulation of Siz2 (Fig. S1 B) and increased Siz2-dependent SUMOylation of previously identified NE targets (Fig. S1 C; Ptak et al., 2021). Consistent with previous observations (Ptak et al., 2021), metaphase-arrested *siz2^{S522A}* cells failed to accumulate siz2^{S522A} (Fig. S1 B) or SUMOylated targets (Fig. S1 C) at the NE. Strikingly, the arrested *siz2^{S522A}* cells had nuclei that lacked nuclear extensions and were largely bispherical (Fig. 1 C, also see Fig. S1 B) with a significantly reduced nuclear surface area relative to a WT counterpart (Fig. 1 D). Similarly, a *scs2^{KI80R}* mutation, which blocks Scs2 SUMOylation and inhibits INM association of Siz2 (Ptak et al., 2021), also showed reduced nuclear surface area (Fig. 1 D). Together, these data suggest that the association of Siz2 with the INM during mitosis supports NE membrane expansion.

Siz2-mediated SUMOylation at the INM induces NE membrane expansion

A cycle of phosphorylation and dephosphorylation during mitosis directs Siz2 binding to and release from the INM (Ptak et al., 2021). To test if association of Siz2 with the NE is sufficient to induce an increase in nuclear surface area independent

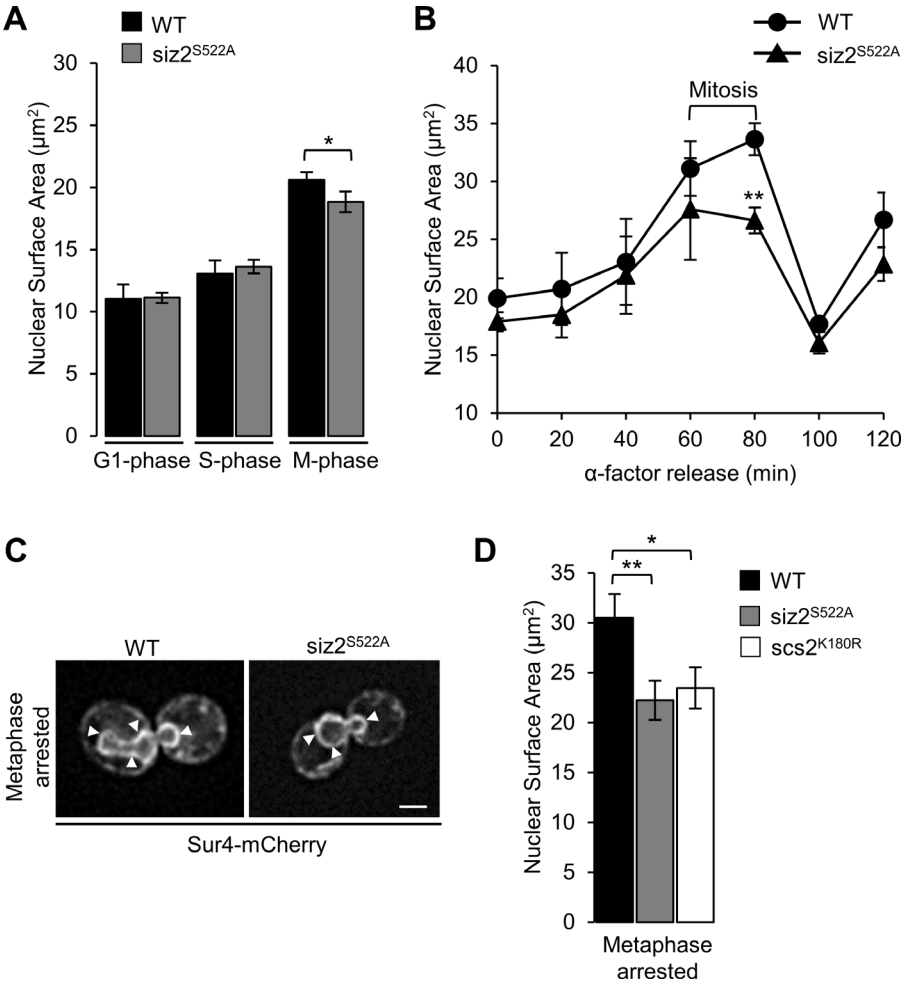

Figure 1. **NE association of Siz2 during mitosis supports NE expansion. (A and B)** Graphs display the average nuclear surface area across cell cycle stages determined from epifluorescence z-stack images of WT and *siz2*^{S522A} cells producing nuclear Pus1-GFP. Nuclear surface areas (µm^2) were measured using Imaris-based surface analysis. For A, asynchronously grown cells were binned into the indicated cell cycle phase based on bud size and nuclear morphology. For B, WT and *siz2*^{S522A} cells were arrested in G1-phase (0 min) using α-factor, released into the cell cycle, and then collected and imaged at the indicated times to determine nuclear surface areas. **(C)** Representative epifluorescence images are shown for WT and *siz2*^{S522A} mutant cells containing integrated *MET3pr-HA$_3$-CDC20* and producing the NE/ER membrane protein marker Sur4-mCherry following metaphase arrest induced by methionine addition for 2 h. Arrowheads point to the NE. Size bar, 2 µm. **(D)** Measured nuclear surface areas of metaphase-arrested cells from the indicated strains as determined in A. Graphs in A, B, and D show data from three biological replicates and 50 cells/replicate/cell cycle stage or time point. Error bars are SD. Asterisks denote a significant change in *siz2*^{S522A} and *scs2*^{K180R} containing cells relative to the WT counterpart as determined using a two-tailed Student's *t* test. *p ≤ 0.05, **p ≤ 0.01.

of the cell cycle, Siz2 was constitutively positioned at the INM using a superfolder split GFP system (Smoyer et al., 2016). For these experiments, *GFP$_{1-10}$* was fused in frame to *SIZ2* to encode Siz2-GFP$_{1-10}$, or, as a control, to a *siz2* mutant containing two point mutations designed to disrupt the RING domain (see Johnson and Gupta, 2001) and block its E3 ligase activity (siz2^{RING}-GFP$_{1-10}$). When nuclear Siz2-GFP$_{1-10}$ protein was coproduced in cells with a fusion protein that contains GFP$_{11}$ positioned on the nucleoplasmic/cytoplasmic face of the ER/NE membrane (GFP$_{11}$-mCherry-TM; Chandra et al., 2021; Smoyer et al., 2016), formation of the GFP$_{1-10}$-GFP$_{11}$ based dimers was visualized at the INM by reconstitution of GFP fluorescence (Fig. 2 A). The GFP signal was detected at the NE in cells at all stages of the cell cycle. Consistent with the INM association of Siz2-GFP$_{1-10}$, higher levels of SUMOylated species normally restricted to mitosis (Fig. S1 A) were detected throughout the cell cycle (Fig. 2 B). By contrast, cells producing Siz2-GFP$_{1-10}$ with GFP$_{11}$ positioned in the ER lumenal network (mCherry-TM-GFP$_{11}$) did not produce an NE GFP signal (Fig. 2 A), nor did these cells show an altered SUMOylation profile (Fig. 2 C). Finally, the GFP$_{11}$-mCherry-TM construct could also direct the siz2^{RING}-GFP$_{1-10}$ mutant to the INM and produce a GFP signal (Fig. 2 D). As predicted, INM binding of this Siz2 ligase dead mutant did not result in increased SUMO conjugates as was detected with Siz2-GFP$_{1-10}$ (Fig. 2 E).

Notably, in cells containing Siz2 constitutively associated with the INM (Siz2-GFP$_{1-10}$-GFP$_{11}$-mCherry-TM), nuclei often appeared misshapen (Fig. 2 A). This phenotype was not observed when Siz2-GFP$_{1-10}$ was not recruited to the INM (mCherry-TM-GFP$_{11}$) or when siz2^{RING}-GFP$_{1-10}$ was bound to the INM (Fig. 2 D). Moreover, Siz2-GFP$_{1-10}$ binding to the INM caused a significant increase in nuclear surface area in cells at each cell cycle stage relative to cells where Siz2-GFP$_{1-10}$ is not recruited to the INM by GFP$_{11}$ (mCherry-TM-GFP$_{11}$; Fig. 2 F) or to cells that produce siz2^{RING}-GFP$_{1-10}$ (Fig. 2 G).

Furthermore, we observed that tethering Siz2-GFP$_{1-10}$ to the INM using the split-GFP system bypasses the requirement for the Siz2 INM-receptor Scs2 (Ptak et al., 2021). A *scs2*^{KI80R} mutant, which blocks Scs2 SUMOylation and inhibits NE association of endogenous Siz2 (Ptak et al., 2021), did not inhibit SUMOylation of other NE targets (Fig. 2 H) nor prevent the nuclear surface area increase caused by anchoring Siz2-GFP$_{1-10}$ to the INM (Fig. 2 I).

Cumulatively, these results show that tethering Siz2 to the INM induces specific SUMOylation events that support NE expansion. We previously showed that cells harboring a specific mutation in the SUMO isopeptidase Ulp1 (*ulp1*$^{K352E/Y583H}$-V5$_3$, referred to here as *ulp1*$^{KE/YH}$) contain higher levels of the mitotic INM SUMO conjugates that persist throughout the cell cycle due

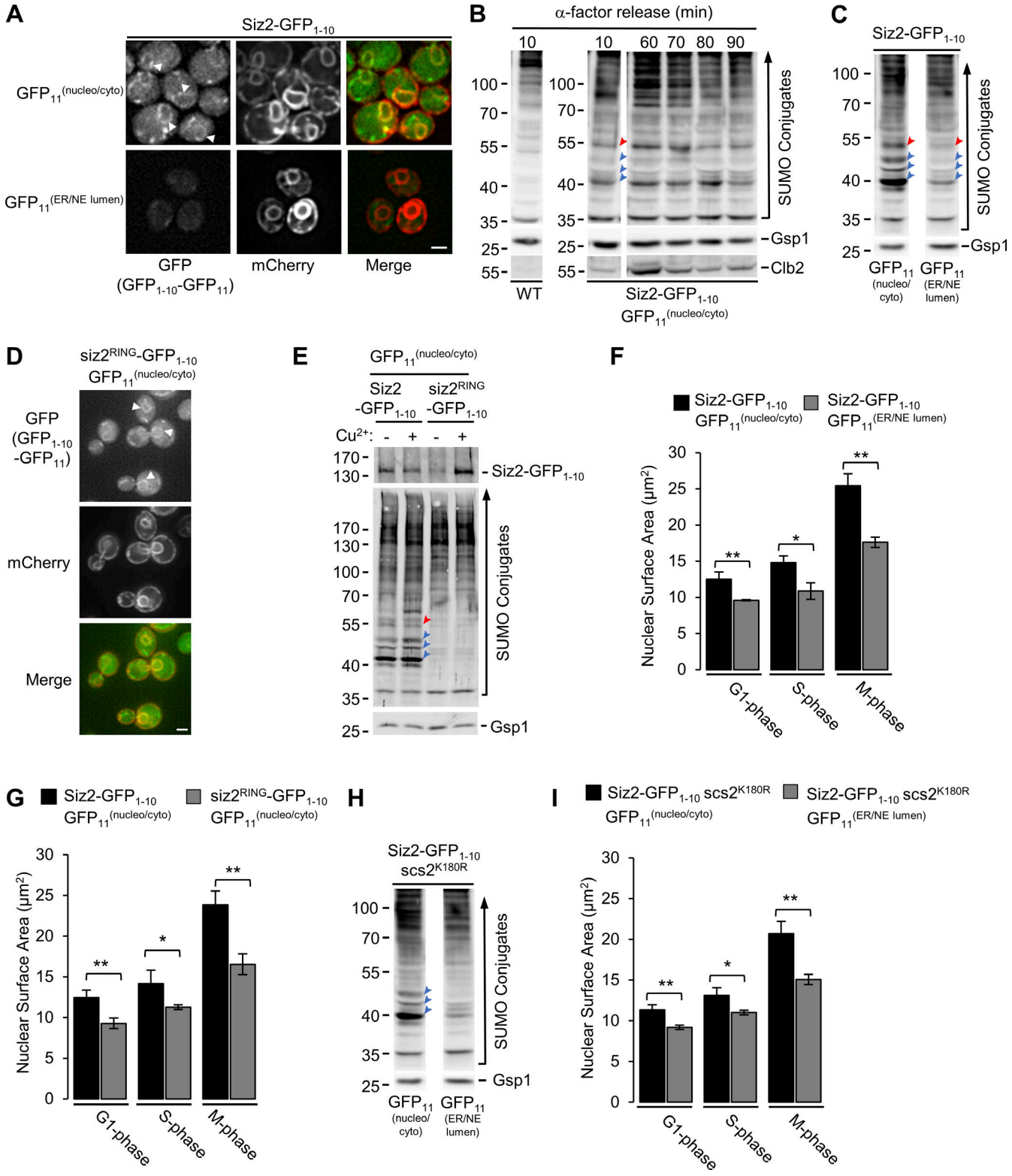

Figure 2. **Constitutive association of Siz2 with the NE induces SUMOylation and increases nuclear surface area. (A)** WT cells producing Siz2-GFP_{1-10} and a plasmid-encoded GFP_{11}-mCherry-TM ($GFP_{11}^{(nucleo/cyto)}$) or mCherry-TM-GFP_{11} ($GFP_{11}^{(NE/ER\ lumen)}$) fusion protein were examined by epifluorescence microscopy. The membrane-integrated GFP_{11} fusion proteins allow for the visualization of NE/ER morphology by mCherry fluorescence. Formation of GFP_{1-10}-GFP_{11} dimers was visualized by GFP fluorescence. Arrowheads point to GFP fluorescence at the NE in several cells. Size bar, 2 µm. **(B)** WT cells or cells producing Siz2-GFP_{1-10} and GFP_{11}-mCherry-TM ($GFP_{11}^{(nucleo/cyto)}$) were arrested in G1-phase using α-factor, released from arrest, and then analyzed every 10 min by Western blotting to detect SUMO conjugates, Clb2, and the Gsp1 load control. Clb2 levels peak in mitosis. Note, Western blot images of samples from the Siz2-GFP_{1-10}/GFP_{11} strain were derived from the same blot. **(C and H)** SUMO conjugate profiles of the indicated strains were assessed by Western blotting of cell lysates derived from asynchronous cultures. Images shown were derived from the same Western blot. **(D)** *siz2Δ* mutant cells containing plasmid-

encoded GFP_{11}-mCherry-TM ($GFP_{11}^{(nucleo/cyto)}$) and a plasmid expressing the *siz2^{RING}-GFP$_{1-10}$* mutant from a copper-inducible promoter were examined by epifluorescence microscopy 4 h after 0.5 mM Cu^{2+} addition. GFP and mCherry fluorescence was visualized as described in A. Arrowheads point to GFP fluorescence at the NE in several cells. Size bars, 2 µm. **(E)** Cultures of cells producing Siz2-GFP_{1-10} and plasmid-encoded GFP_{11}-mCherry-TM ($GFP_{11}^{(nucleo/cyto)}$) and *siz2Δ* mutant cells producing plasmid-encoded siz2^{RING}-GFP_{1-10} and GFP_{11}-mCherry-TM ($GFP_{11}^{(nucleo/cyto)}$) (described in D) were incubated in the presence or absence of 0.5 mM Cu^{2+} for 4 h. SUMO conjugates and the GFP_{1-10} fusions were detected by Western blotting. Note, following induction, the *CUP1pr-siz2^{RING}-GFP$_{1-10}$* gene produced levels of siz2^{RING}-GFP_{1-10} similar to Siz2-GFP_{1-10}. **(F and I)** Nuclear surface areas of WT (F) and *scs2^{K180R}* mutant (I) cells expressing the specified constructs at the indicated cell cycle stage were determined using Pus1-GFP as described in Fig. 1 A. **(G)** Pus1-GFP was introduced into the two strains described in E and nuclear surface areas of cells were examined after Cu^{2+} induction. Note, arrowheads on Western blots in B, C, E, and H point to SUMOylated Scs2 (red) and/or three prominent Siz2-dependent INM SUMO conjugates (blue; Ptak et al., 2021). Mass markers are shown in kilodaltons. Error bars for all graphs shown are SD, and p values were determined using a two-tailed Student's *t* test for the indicated sample pairs. *p ≤ 0.05, **p ≤ 0.01. Source data are available for this figure: SourceData F2.

to a reduction in their deSUMOylation (Ptak et al., 2021). Consistent with this observation, immunofluorescence microscopy analysis of the *ulp1$^{KE/YH}$* mutant showed increased levels of SUMO at the NE in interphase cells that were absent in a *ulp1$^{KE/YH}$ siz2^{S522A}* double mutant (Fig. 3 A). The increased levels of SUMO at the NE in interphase *ulp1$^{KE/YH}$* mutant cells were not due to a persistent localization of Siz2 to the INM (Fig. S2). Importantly, as we observed in cells constitutively tethering Siz2-GFP_{1-10} to the INM (Fig. 2 A), the nuclei of *ulp1$^{KE/YH}$* mutant cells appeared misshapen and often exhibited NE extensions (Fig. 3, A and B). Consistent with this observation, *ulp1$^{KE/YH}$* mutant cells showed an increased nuclear surface area relative to WT cells at all cell cycle stages examined (Fig. 3 C). Preventing Siz2 recruitment to the INM (*ulp1$^{KE/YH}$ siz2^{S522A}* or *ulp1$^{KE/YH}$ scs2^{K180R}*) restored the spherical appearance of nuclei and the nuclear surface area to WT levels in G1- and S-phase cells (Fig.3, B and C). The nuclear surface areas of M-phase *ulp1$^{KE/YH}$ siz2^{S522A}* and *ulp1$^{KE/YH}$ scs2^{K180R}* mutant cells were reduced relative to WT cells and were similar to values observed in the *siz2^{S522A}* mutant (Fig. 1 A and Fig. 3 C). Together, these data led us to conclude that Siz2 INM localization and SUMOylation of associated targets, including Scs2, direct NE expansion during mitosis.

Siz2-mediated SUMOylation increases INM levels of PA during mitosis

PA is a key precursor for phospholipids. Conditions predicted to increase levels of PA produce NE abnormalities, prompting the hypothesis that increased PA levels support NE membrane expansion during mitosis (Kwiatek et al., 2020; Santos-Rosa et al., 2005). With this model in mind, potential changes in PA levels at the NE and their relationship to Siz2 and SUMOylation were investigated during the cell cycle. A nuclear-localized PA sensor (NLS-PA sensor-mCherry) was used to detect PA at the INM using fluorescence microscopy (Romanauska and Köhler, 2018). As expected, the NLS-PA sensor was predominantly nuclear in WT interphase cells (Fig. 4 A). However, in mitotic cells, both those in asynchronous cultures (Fig. 4 B) and Cdc20-depleted metaphase-arrested cultures (Fig. 4 C), the NLS-PA sensor was enriched at the NE, consistent with increased PA levels in the INM. The mitotic increase of the NLS-PA sensor at the INM was dependent on the INM association of Siz2 and/or SUMOylation of Siz2-dependent targets as the sensor was not detected at the INM in *siz2^{S522A}* or *scs2^{K180R}* mutant cells (Fig. 4, B and C). These SUMO-dependent, mitotic changes in PA levels were only seen at the INM, and no changes in plasma membrane PA levels were detected using a cytoplasmic PA sensor (Fig. S3, A and B).

Tethering Siz2-GFP_{1-10} to the INM using GFP_{11}-mCherry-TM (see Fig. 2) also led to an additional interphase enrichment of the NLS-PA sensor at the INM (Fig. 5 A). This increase in INM PA coincided with increased nuclear surface areas detected throughout the cell cycle in Siz2-INM tethered cells (see Fig. 2 F). Finally, *ulp1$^{KE/YH}$* mutant cells were examined using the NLS-PA sensor, and they similarly showed increased localization of the sensor to the INM in both interphase and mitotic cells, indicating an accumulation of PA at the INM in the *ulp1$^{KE/YH}$* mutant (Fig. 5 B). By contrast, *ulp1$^{KE/YH}$* mutant cells containing the *siz2^{S522A}* mutation showed no enrichment of PA at the INM (Fig. 5 C). Cumulatively, these results directly implicate Siz2-mediated SUMOylation events in the enrichment of PA at the INM during mitotic NE expansion.

Siz2-directed NE membrane expansion is linked to Pah1 activity

Steady-state PA levels are regulated, in part, by the phosphatase Pah1, which dephosphorylates PA to yield DAG (Kwiatek et al., 2020). Notably, previous studies have linked the inhibition of Pah1 activity and an accompanying increase in PA levels to NE expansion (Han et al., 2006; Santos-Rosa et al., 2005). For example, loss of the Pah1 activators Spo7 and Nem1 results in unregulated NE expansion (Santos-Rosa et al., 2005; Siniossoglou et al., 1998; Webster et al., 2010). Moreover, the inhibition of Pah1 during mitosis by cyclin-dependent kinase (Cdk)-mediated phosphorylation has been proposed to reduce the membrane association of Pah1, leading to increased PA levels and NE expansion (Choi et al., 2011; Santos-Rosa et al., 2005). Consistent with this idea, a *pah1^{7A}* mutant, which contains mutations that prevent mitotic phosphorylation, exhibits increased membrane binding, elevated phosphatidate phosphatase activity in vitro (Choi et al., 2011; O'Hara et al., 2006), and its expression in *spo7Δ* and *nem1Δ* null mutants suppresses their NE expansion phenotypes (Choi et al., 2011). These studies led us to examine whether the Siz2-dependent increase in mitotic INM PA was linked to the inhibition of Pah1 activity. Consistent with this mechanism, using a previously characterized sensor of INM DAG (NLS-DAG sensor; Romanauska and Köhler, 2018), we observed in WT cells that, in contrast to the increase in PA levels (Fig. 4 B), the NLS-DAG sensor detected decreased levels of DAG at the INM in mitotic cells relative to that seen in interphase cells (Fig. S3 C). Importantly, unlike WT cells, *siz2^{S522A}* mutant cells, which fail to accumulate PA at the INM,

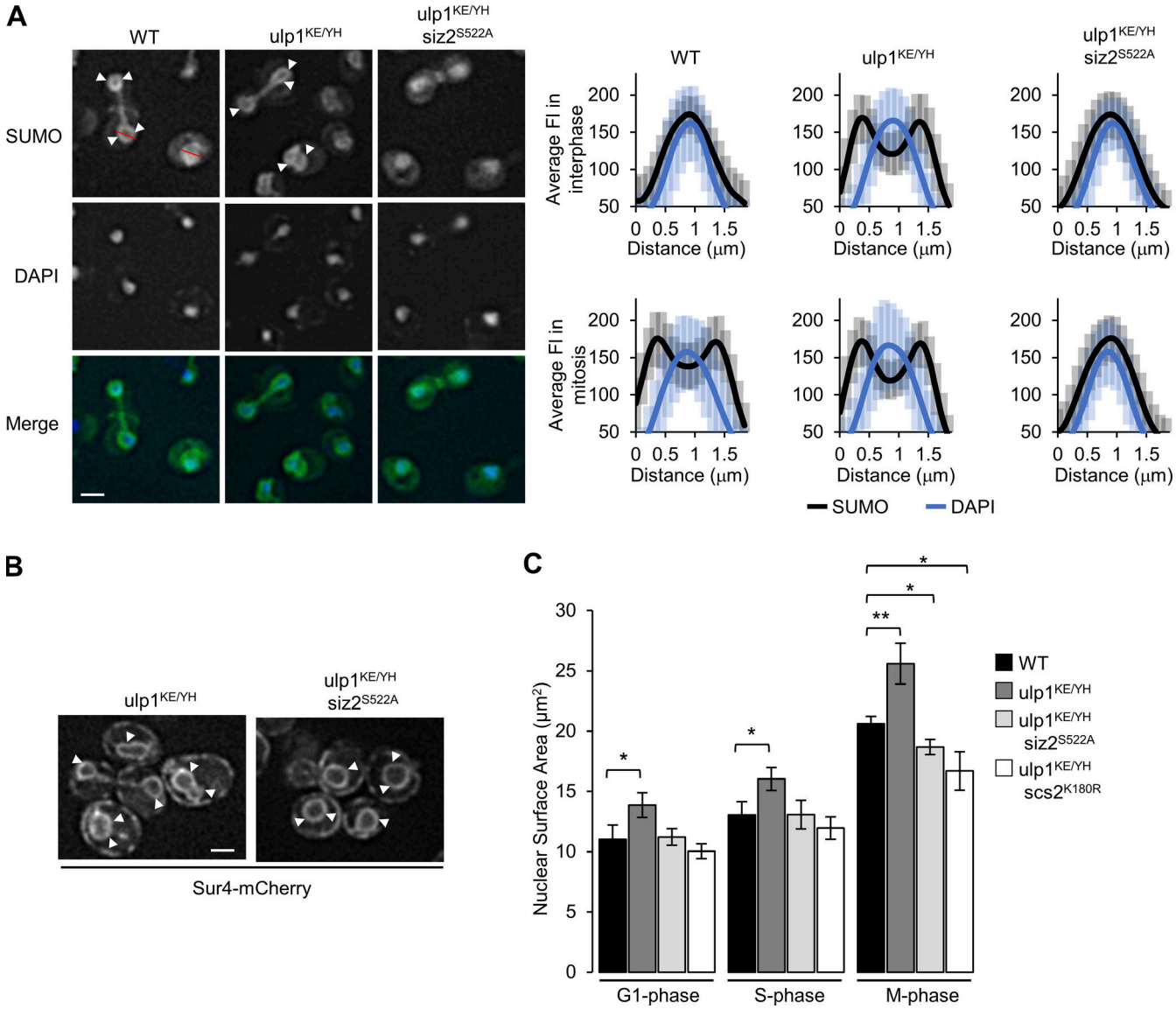

Figure 3. **Ulp1 restricts nuclear membrane expansion. (A)** Anti-SUMO immunofluorescence analysis of WT, *ulp1*$^{K352E/Y583H}$-V5$_3$ (termed *ulp1*$^{KE/YH}$), and *ulp1*$^{KE/YH}$ *siz2*^{S522A} mutant cells. Arrowheads highlight SUMO along the NE, with nuclear position determined by DAPI staining. Nuclear distribution of anti-SUMO immunofluorescence relative to a DAPI signal was determined using line scan intensities of equatorial optical sections through the nuclei (see red line for example) of interphase (unbudded or small budded) and mitotic (large budded) cells. Each plot shows average fluorescence intensity (FI) for anti-SUMO immunofluorescence signal and DAPI at multiple points along a 1.85-μm line for n = 25 nuclei. Size bar, 2 μm. Error bars are SD. **(B)** Representative epi-fluorescence images of *ulp1*$^{KE/YH}$ and *ulp1*$^{KE/YH}$ *siz2*^{S522A} mutant cells producing the NE/ER marker Sur4-mCherry. Size bar, 2 μm. Arrowheads point to the NE. **(C)** Nuclear surface area of the indicated strains was determined using Pus1-GFP as described in Fig. 1 A at the indicated cell cycle stage. Note, the results shown here and in Fig. 1 A were obtained at the same time, and the data from the WT strain are reproduced here. The data represent three biological replicates and n = 50 cells/replicate/cell cycle stage. Error bars are SD. P values were determined using a two-tailed Student's t test for the indicated sample pairs. *p ≤ 0.05, **p ≤ 0.01.

showed increased levels of INM DAG during mitosis and upon metaphase arrest (Fig. S3, D and E). These results are consistent with INM SUMOylation functioning to inhibit Pah1 activity.

Several additional approaches were used to further assess the functional relationship between SUMOylation and Pah1 with respect to the regulation of INM PA levels and NE membrane expansion. First, we tested whether exogenous expression of the *pah1*^{7A} mutant would inhibit PA accumulation at the INM and reduce nuclear surface area in metaphase-arrested (Cdc20-depleted) cells. Expression of the *pah1*^{7A} mutant, but not *PAH1*, reduced the INM accumulation of the NLS-PA sensor and the nuclear surface area of arrested cells (Fig. 6, A and B). Notably, the expression of exogenous *pah1*^{7A} or WT *PAH1* did not affect SUMOylation in metaphase-phase arrested cells (Fig. S3 F). Similarly, in asynchronous cell cultures, expression of the *pah1*^{7A} mutant, but not *PAH1*, prevented mitotic increases of the NLS-PA sensor at the INM and reduced the nuclear surface area in cells at all stages of the cell cycle (Fig. 6, C and D).

Phenotypes arising from expression of the constitutively active *pah1*^{7A} mutant parallel those detected in cells where

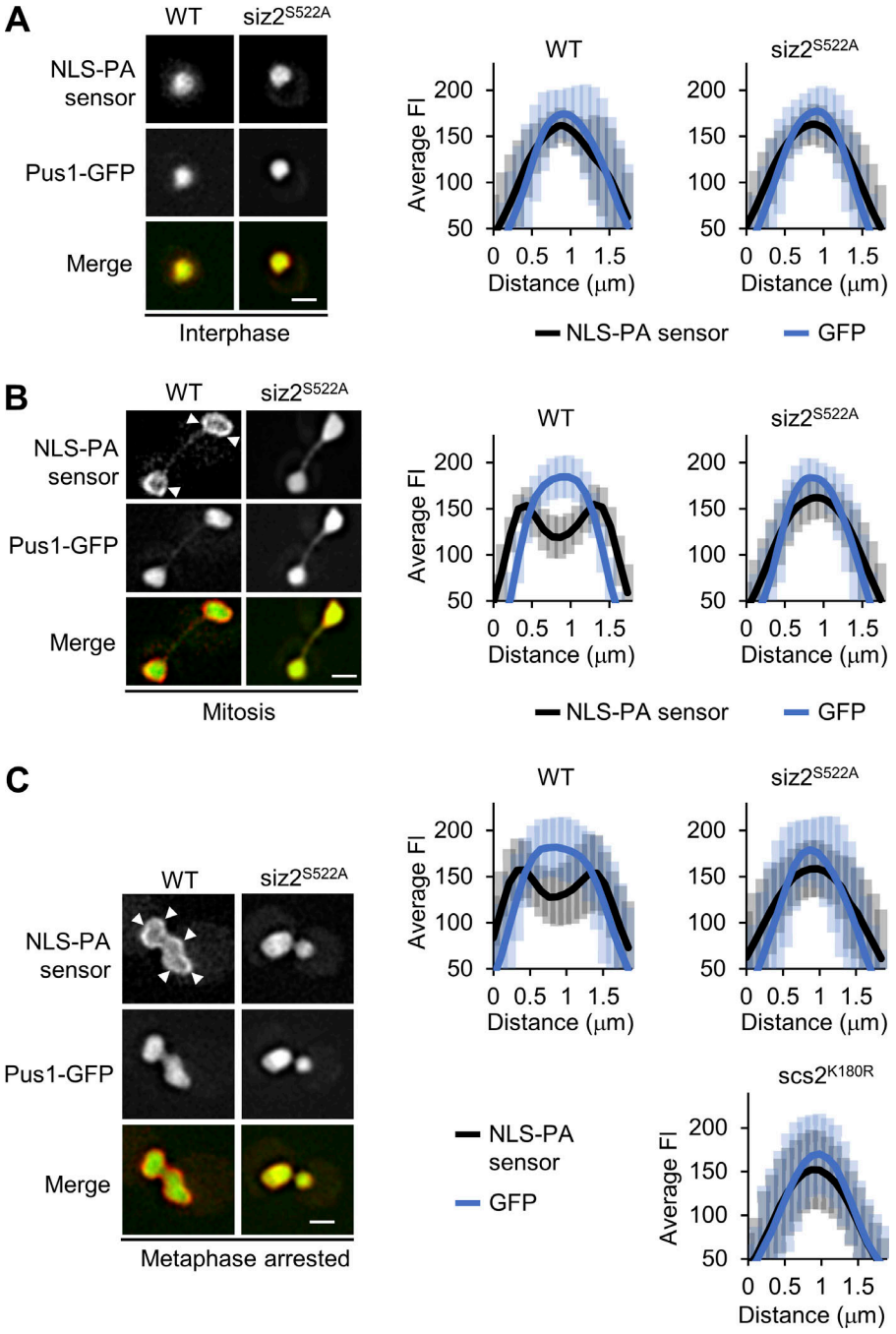

Figure 4. **The NE association of Siz2 during mitosis is required for enrichment of PA at the INM.** WT and *siz2*^{S522A} mutant cells producing Pus1-GFP and a nuclear NLS-PA sensor protein (NLS-Opi1(Q2)-mCherry) were examined by epifluorescence microscopy. **(A and B)** Representative images of interphase (A) and mitotic (B) cells in actively growing cultures are shown. **(C)** A *MET3pr-HA*$_3$*-CDC20* cassette was integrated into WT, *siz2*^{S522A}, and *scs2*^{K180R} strain backgrounds. These cells were arrested in metaphase by methionine addition for 2 h and the localization of the NLS-PA sensor and Pus1-GFP was examined. In each panel, nuclear distribution of the NLS-PA sensor protein (mCherry) and Pus1-GFP was determined using line scan intensities as described in the Fig. 3 A legend. Arrowheads highlight the NLS-PA sensor along the INM. Error bars are SD. Size bar, 2 μm.

mitotic INM SUMOylation is inhibited (i.e., *siz2*^{S522A} mutant; Figs. 1 and 4), consistent with our hypothesis that SUMOylation at the INM suppresses the activity of Pah1 during mitosis. To further investigate this relationship, we examined whether the NE membrane phenotypes seen in *siz2*^{S522A} and *ulp1*$^{KE/YH}$ mutants were functionally linked to Pah1 and levels of PA. First, we examined whether suppression of mitotic NE membrane expansion by the *siz2*^{S522A} mutant was dependent on the activation of Pah1 using cells lacking its activator Spo7. As shown in Fig. 7 A, the *spo7*Δ mutant suppressed the expansion defect observed in the *siz2*^{S522A} mutants, consistent with *siz2*^{S522A}-mediated inhibition of NE expansion being dependent on Spo7 and activation of Pah1.

We next examined whether the NE expansion phenotype of *ulp1*$^{KE/YH}$ mutant cells was dependent on the inhibition of Pah1. First, we examined if introducing the exogenous *pah1*^{7A} gene could suppress the NE expansion phenotype of *ulp1*$^{KE/YH}$ mutant cells (see Fig. 3). Upon expression of *pah1*^{7A}, but not *PAH1*, the INM accumulation of PA (Fig. 7 B) and nuclear surface areas in interphase and mitotic *ulp1*$^{KE/YH}$ mutant cells (Fig. 7 C) were reduced. Moreover, the nuclear surface area values in WT and *ulp1*$^{KE/YH}$ mutant cells expressing the *pah1*^{7A} mutant were indistinguishable (Fig. 6 D). Of note, the expression of *pah1*^{7A} (or control *PAH1*) did not affect SUMOylation levels in *ulp1*$^{KE/YH}$ mutant cells (Fig. S3 G).

Finally, we tested whether activation of endogenous Pah1 would suppress the NE expansion phenotype of the *ulp1*$^{KE/YH}$

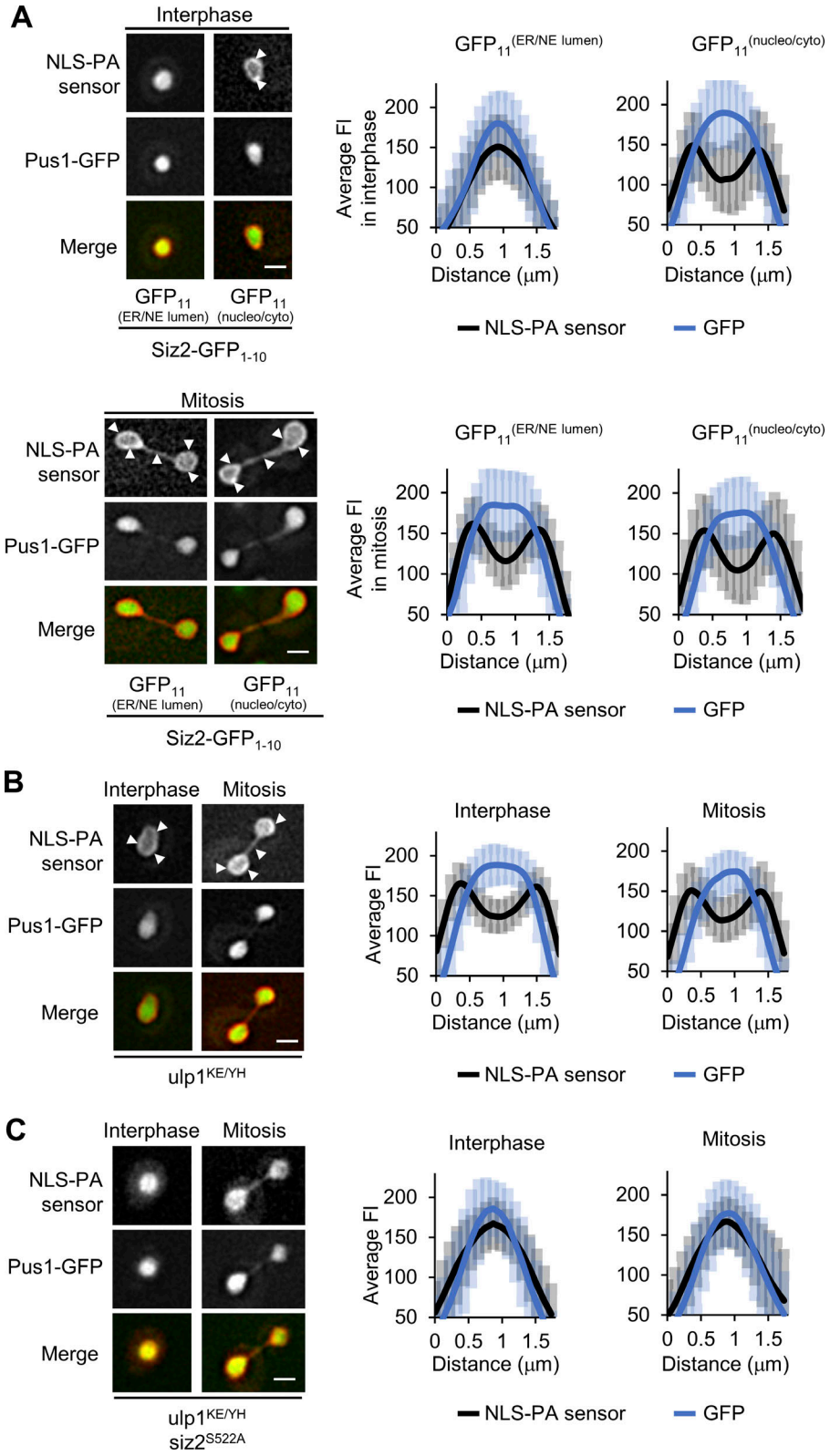

Figure 5. **INM enrichment of PA is induced by Siz2-mediated NE SUMOylation. (A)** WT cells producing nucleoplasmic Pus1-GFP, the NLS-PA sensor (mCherry), and Siz2-GFP_{1-10} along with either the plasmid-encoded GFP_{11}-TM ($GFP_{11}^{(nucleo/cyto)}$) or TM-GFP_{11} ($GFP_{11}^{(NE/ER\ lumen)}$) reporter were examined by epifluorescence microscopy. Images show the localization of Pus1-GFP and the NLS-PA sensor (mCherry) in representative interphase and mitotic cells from actively growing cultures. Arrowheads point to the NLS-PA sensor enriched at the NE. Note, the NE signal of the Siz2-GFP_{1-10}-$GFP_{11}^{(nucleo/cyto)}$ dimer is not visible due to the abundance of nucleoplasmic Pus1-GFP. **(B and C)** The nuclear distribution of the NLS-PA sensor protein (mCherry) and Pus1-GFP was similarly examined in interphase and mitotic cells present in asynchronous cultures of *ulp1*$^{KE/YH}$ (B) and *ulp1*$^{KE/YH}$ *siz2*^{S522A} (C) mutant strains. Arrowheads highlight the NLS-PA sensor protein along the INM. The nuclear distributions of the NLS-PA sensor protein (mCherry) and Pus1-GFP were determined using line scan intensities (n = 25 nuclei) as described in the Fig. 3 A legend. Error bars are SD. Size bar, 2 μm.

mutant. To do this, we deleted an inhibitor of the Spo7/Nem1 complex, Ice2, which results in increased Pah1 activity (Papagiannidis et al., 2021). The *ice2*Δ mutant suppressed the NE expansion phenotype of the *ulp1*$^{KE/YH}$ mutant cells (Fig. 7 D). Similarly, loss of Dgk1, which functions to phosphorylate DAG and produce PA, also suppressed the membrane expansion phenotype of the *ulp1*$^{KE/YH}$ mutant cells (Fig. 7 E). Cumulatively, these results are consistent with our proposed role for SUMOylation in regulating PA levels by inhibiting the Pah1-Spo7/Nem1 complex.

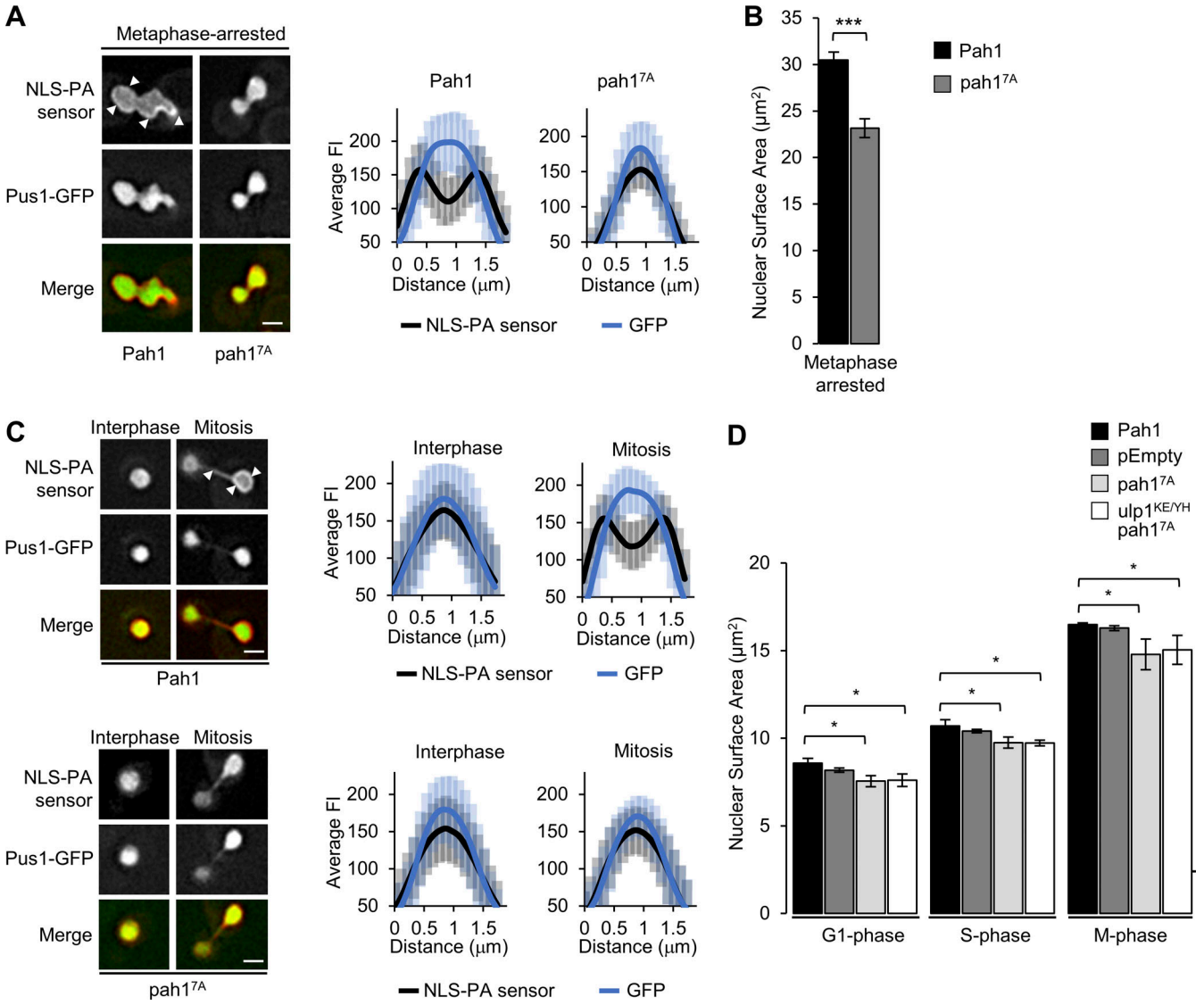

Figure 6. **Pah1 activity antagonizes Siz2-mediated increases in nuclear surface area. (A)** WT cells producing Pus1-GFP, the nuclear NLS-PA sensor protein, and containing integrated *MET3pr-HA$_3$-CDC20* were transformed with plasmids containing *PAH1-PrA* or the *pah1^{7A}-PrA* mutant gene. Note that these protein A (PrA) fusions are designated simply as Pah1 and pah1^{7A} throughout the figure. Cells were arrested in metaphase by methionine addition for 2 h, and the localization of the NLS-PA sensor and Pus1-GFP were examined by epifluorescence microscopy. A representative image of a metaphase-arrested cell is shown for each strain (left; Size bar, 2 µm). Arrowheads highlight the NLS-PA sensor protein along the INM. The nuclear distributions of the NLS-PA sensor protein (mCherry) and Pus1-GFP were determined using line scan intensities (right, *n* = 25 nuclei) as described in the Fig. 3 A. Error bars are SD. **(B)** These same strains were arrested in metaphase and the nuclear surface area of individual cells was determined using Pus1-GFP as described for Fig. 1 A. The data represent three biological replicates and *n* = 50 cells/replicate/cell cycle stage. Error bars are SD, and p values were determined using a two-tailed Student's *t* test for the indicated sample pairs. ***p ≤ 0.001. **(C)** WT cells producing Pus1-GFP, and a nuclear NLS-PA sensor protein, were transformed with plasmids containing *PAH1-PrA* or the *pah1^{7A}-PrA* mutant. Cells from asynchronously growing cultures were examined by epifluorescence microscopy and representative images of interphase and mitotic cells are shown (left, size bar, 2 µm). Arrowheads highlight the NLS-PA sensor protein at the INM. Nuclear distributions of the NLS-PA sensor protein and Pus1-GFP were quantified as in A. **(D)** Nuclear surface areas of WT or the *ulp1$^{KE/YH}$* mutant cells expressing exogenous *PAH1-PrA* or the *pah1^{7A}-PrA* mutant were determined at the indicated cell cycle stage using Pus1-GFP as described in Fig. 1 A. The data represent three biological replicates and *n* = 50 cells/replicate/cell cycle stage. Error bars are SD. Asterisks indicate a significant difference relative to WT cells expressing exogenous *PAH1* as determined using a two-tailed Student's *t* test. *p ≤ 0.05.

Siz2 regulates the interactions of Pah1, Nem1, and Spo7

The binding of Pah1 to membranes is mediated by interactions with the Spo7/Nem1 integral membrane phosphatase complex, which dephosphorylates Pah1 and promotes its membrane association (Dubots et al., 2014; Karanasios et al., 2010). On the basis of our results, we hypothesized that Siz2-mediated SUMOylation drives PA increases at the INM during mitosis by reducing Pah1 association with the Spo7/Nem1 complex. Consistent with this idea, in addition to the ER, Pah1 is detected in the nucleoplasm and at the INM (Romanauska and Köhler, 2018), and we detect the presence of both Spo7 and Nem1 at the INM using the superfolder split GFP system (Fig. S4 A). Thus, co-affinity purification analysis was used to assess the level of Pah1 binding to the Spo7/Nem1 complex during

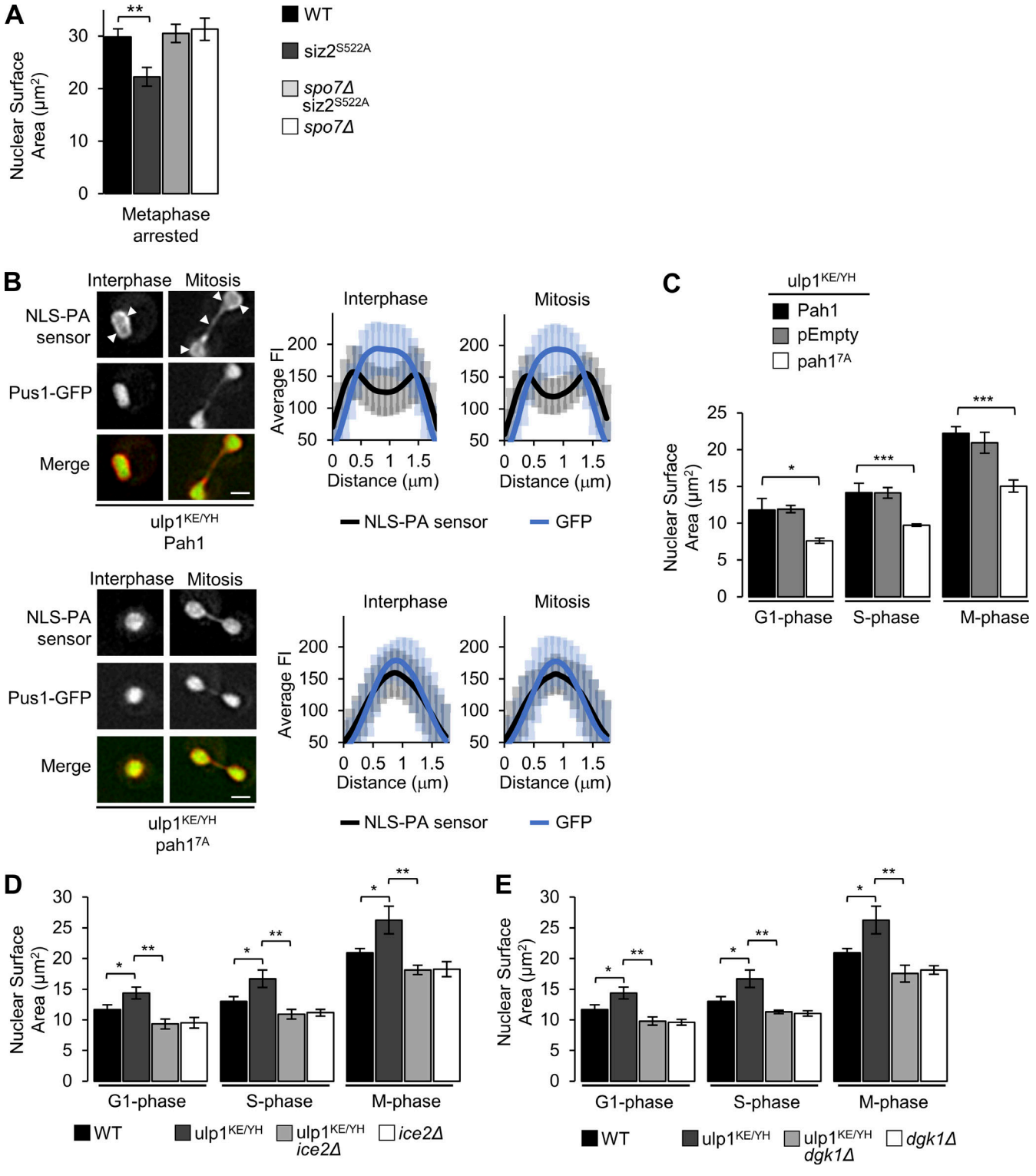

Figure 7. **Phenotypes associated with altered INM SUMOylation are functionally linked to Pah1 activity. (A)** Indicated strains containing *MET3pr-HA$_3$-CDC20* and producing Pus1-GFP were arrested in metaphase by the depletion of Cdc20. Nuclear surface areas of metaphase-arrested cells were determined as described for Fig. 1 A. **(B)** *ulp1$^{KE/YH}$* mutant cells producing Pus1-GFP, and the NLS-PA sensor protein, were transformed with plasmids containing *PAH1-PrA* or the *pah1^{7A}-PrA* mutant. Note, these protein A (PrA) fusions are designated simply as Pah1 and pah1^{7A}. Representative images of interphase and mitotic cells in actively growing cultures are shown. Arrowheads highlight the NLS-PA sensor protein along the INM. The nuclear distributions of the NLS-PA sensor and Pus1-GFP (n = 25 nuclei) were determined using line scan intensities as described in the Fig. 3 A legend. Error bars are SD. Size bar, 2 μm. **(C–E)** Nuclear surface areas of the indicated strains from asynchronous cultures were determined using Pus1-GFP as described for Fig. 1 A. Data in D and E were obtained at the same time and data for WT and *ulp1$^{KE/YH}$* samples are reproduced in both panels for comparison. Data in A and C–E are from three biological replicates per strain, with 50 cells/replicate/cell cycle stage. Error bars are SD. Asterisks denote significant change in nuclear surface area relative to the indicated counterpart as determined using a two-tailed Student's t test. *p ≤ 0.05, **p≤ 0.01, ***p ≤ 0.001.

interphase (G1-phase) and to determine whether these interactions were altered during mitosis. Because Spo7 mediates Pah1 interactions with the Spo7/Nem1 complex (Dubots et al., 2014; Siniossoglou et al., 1998), Spo7-TAP was purified from cell lysates to assess interactions of Pah1 with the Spo7/Nem1 complex. For these experiments, cell cultures were synchronized in the G1-phase using α-factor and then examined directly (0 min after release) or released from arrest and sampled in mitosis (60 min after release). Levels of Spo7-TAP in whole cell lysates were similar in G1-phase (α-factor arrest) and M-phase (60 min after α-factor release; Fig. S4 B). In addition, mitotic interactions were evaluated in cells arrested in metaphase by Cdc20 depletion. In G1-phase cells, Pah1 was detected in association with Spo7-TAP, but in mitotic extracts (both 60 min after α-factor release and following Cdc20 depletion) the amount of Pah1 bound to Spo7-TAP was significantly reduced (Fig. 8, A and B). Importantly, this reduction in Pah1 association with Spo7 seen in WT cells was not observed in *siz2*^{S522A} mutant cells; rather, levels of Pah1 bound to Spo7 in mitotic extracts from this mutant were similar to, or higher than, that detected in G1-phase extracts (Fig. 8, C and D). Notably, the electrophoretic mobility of Pah1 in mitotic *siz2*^{S522A} mutant cells did not appear to be altered relative to its WT counterpart, suggesting the increased binding of Pah1 to Spo7 in the mutant may not be due to changes in Pah1 phosphorylation (Fig. S3 H). These results suggest that the interaction of the Spo7/Nem1 complex with Pah1 is inhibited during mitosis, and SUMOylation at the NE suppresses their association.

The Spo7/Nem1 complex is required for the membrane association and activation of Pah1 (Santos-Rosa et al., 2005; Siniossoglou et al., 1998). Therefore, the interaction of Spo7 with Nem1 was assessed during mitosis, when the activity of the Spo7/Nem1 complex is predicted to be reduced based on increased PA levels and NE expansion. The binding of Spo7-TAP to Nem1 was examined under the same cell cycle conditions described for Spo7-TAP binding to Pah1 (Fig. 8). In line with the Spo7/Nem1 complex being less active, the levels of Nem1 bound to Spo7-TAP in synchronized cultures of WT cells in mitosis (Fig. 9 A) or cells arrested in metaphase (Fig. 9 B) were significantly reduced when compared to that detected in G1-phase cells. Importantly, the reduced association of Spo7 with Nem1 seen in mitotic WT cells was not detected in *siz2*^{S522A} mutant cells (Fig. 9, C and D), consistent with the lack of NE expansion seen in *siz2*^{S522A} mutant cells as compared to WT (Fig. 1).

The reduced binding of Spo7 to Pah1 and Nem1 during mitosis was not a general property of all Spo7 interacting partners. Similar IP experiments were performed to examine the interaction of Spo7-TAP with another of its binding partners Ice2 (Papagiannidis et al., 2021). As shown in Fig. S4 C, similar levels of Ice2 were detected bound to Spo7-TAP in G1-phase and metaphase-arrested cells suggesting that Spo7 interactions with Pah1 and Nem1 were specifically reduced during mitosis.

As our data suggested that Siz2-mediated SUMOylation at the INM inhibits the interactions of Spo7 with Pah1 and Nem1, we predicted that constitutively higher levels of Siz2-mediated SUMOylation observed throughout the cell cycle in *ulp1*$^{KE/YH}$ mutant cells would result in a general reduction in the interactions of Spo7 with Pah1 and Nem1. Using co-affinity purification analysis, the binding of Spo7-TAP to Pah1 and Nem1 were measured in asynchronous cultures and found to be significantly reduced in *ulp1*$^{KE/YH}$ mutant cells (Fig. 10). In line with this being directly related to Siz2 activity at the INM, these interactions were increased in an *ulp1*$^{KE/YH}$ *siz2*^{S522A} double mutant when compared to the *ulp1*$^{KE/YH}$ mutant (Fig. 10). Cumulatively, these observations support a model in which Siz2-mediated mitotic SUMOylation inhibits formation of the Pah1/Spo7/Nem1 complex and promotes PA accumulation at the INM and NE expansion.

Discussion

A mitotic wave of INM protein SUMOylation regulates numerous cell cycle events, including the reformation of chromatin interactions with the INM in newly forming nuclei (Ptak et al., 2021). Here, we have shown that Siz2 SUMOylation also supports NE membrane growth during this same time period, thus coordinating chromatin attachment to the INM with NE expansion as the interphase nuclear structure is re-established in mother and daughter cells. We show that binding of Siz2 to the INM and the resulting SUMOylation events increase levels of the phospholipid precursor PA at the INM and drive NE membrane expansion during mitosis. On the basis of our results, we propose that the increase in INM PA levels requires the Siz2-dependent inhibition of Pah1 activity resulting from the reduced binding of Pah1 to its activating Spo7/Nem1 complex.

As a cell proceeds from mitosis into the G1-phase, the re-establishment of interphase nuclear architecture in the two daughter cells is accompanied by a doubling of NE membrane surface area. In the closed mitosis of budding yeast, this process is detected as an increase in nuclear surface area as the cell progresses through mitosis (Wang et al., 2016; see Fig. 1 B). Strikingly, when a cell is arrested in metaphase by, for example, spindle assembly checkpoint arrest, NE membrane production continues in the arrested cell. This leads to extensive distortions of the nuclear surface and an increase in nuclear surface area (Witkin et al., 2012; see Fig. 1).

Mitotic NE membrane expansion has been previously linked to the downregulation of Pah1 activity, an event predicted to increase PA levels and its use as a phospholipid precursor (Santos-Rosa et al., 2005). Loss of Pah1 (*pah1*Δ) or the Pah1-activating complex Spo7/Nem1 (*spo7*Δ and *nem1*Δ) leads to expansion of the NE membrane and the appearance of NE membrane extensions visible throughout the cell cycle (Campbell et al., 2006; Choi et al., 2011; Han et al., 2008; Santos-Rosa et al., 2005; Siniossoglou et al., 1998; Witkin et al., 2012). These observations, coupled with data showing the mitotic phosphorylation of Pah1 and the apparent role of this modification in inhibiting Pah1 activity and membrane association, led to a proposed role for Pah1 inhibition in mitotic NE expansion (Choi et al., 2011; Choi et al., 2012; O'Hara et al., 2006; Santos-Rosa et al., 2005). A recent study in the fission yeast *Schizosaccharomyces pombe* also reported a decrease in INM DAG associated with NE expansion during mitosis, which was ascribed, in part, to the inhibition of the *S. pombe* counterpart of Pah1 (Foo et al., 2023).

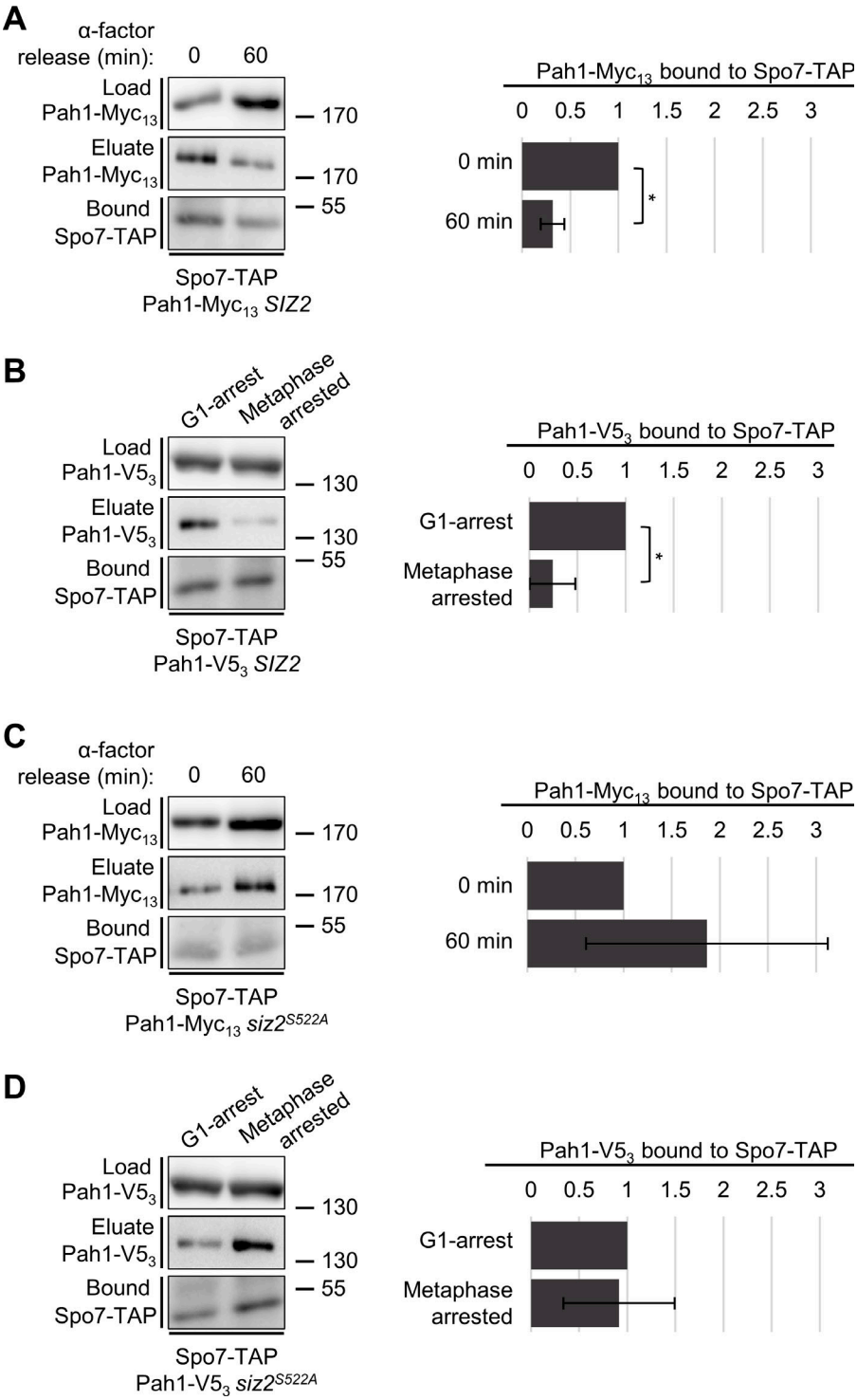

Figure 8. **Binding of Siz2 to the INM during mitosis inhibits the interaction of Pah1 with the Spo7/Nem1 complex. (A and C)** WT (*SIZ2*) and *siz2*^{S522A} mutant cells, each expressing *SPO7-TAP* and *PAH1-MYC*$_{13}$, were arrested in G1-phase with α-factor (0 min) and then released from arrest and allowed to proceed into mitosis (60 min after release). At 0 and 60 min after release, equal amounts of cells were lysed and Spo7-Tap was affinity-purified from lysate fractions (Load). Pah1-Myc$_{13}$ was released from purified Spo7-Tap using sequential $MgCl_2$ elution steps, which were then pooled into a single fraction (Eluate). Bead-bound Spo7-Tap was finally released with 0.5 M acetic acid (Bound; see Materials and methods for details). Equivalent percentages of the load, eluate, and bound fractions were examined by Western blotting (WB) to detect the TAP and Myc$_{13}$ tag. **(B and D)** The same purification and analysis procedures described above were used to analyze Spo7-TAP-bound Pah1-V5$_3$ in WT (*SIZ2*) and *siz2*^{S522A} cells (each containing the *MET3pr-HA*$_3$*-CDC20* cassette) and arrested in G1-phase with α-factor or in metaphase by the depletion of Cdc20 (2 h after methionine addition). Mass markers are shown in kilodaltons. Adjacent bar graphs in each panel show the average relative ratio of Pah1 bound (Eluate) to purified Spo7-TAP (Bound) from three affinity purification experiments, with the ratio of Pah1 to Spo7-TAP in G1 cells (0 min and G-1 arrested) assigned a value of 1 (see Materials and methods). Error bars are SD, and p values were determined using a Student's paired *t* test. **p ≤ 0.01. Source data are available for this figure: SourceData F8.

Our data further support a link between the regulation of PA metabolism and mitotic NE membrane expansion. During mitosis, we detected elevated levels of PA at the INM using a nucleoplasmic PA sensor (Fig. 4). Importantly, this enrichment of PA at the INM was strictly dependent on the phosphorylation-dependent relocalization of Siz2 to the INM (Ptak et al., 2021; Fig. 4), suggesting SUMOylation of an INM target(s) triggers mitotic PA accumulation. Further supporting this conclusion, we observed that constitutively tethering Siz2, but not a ligase defective mutant (*siz2*^{RING}; Fig. 2), to the INM using split superfolder GFP fusions induced the same events seen during mitotic relocalization of Siz2 to the INM to occur throughout the cell cycle, including SUMOylation of INM targets, increased PA levels at the INM, and NE expansion (Fig. 2 and Fig. 5 A). We conclude from these results that Siz2 association with the INM and the accompanying SUMOylation events are required to support increases in INM PA levels and NE expansion during mitosis. Furthermore, these events can be induced by Siz2-

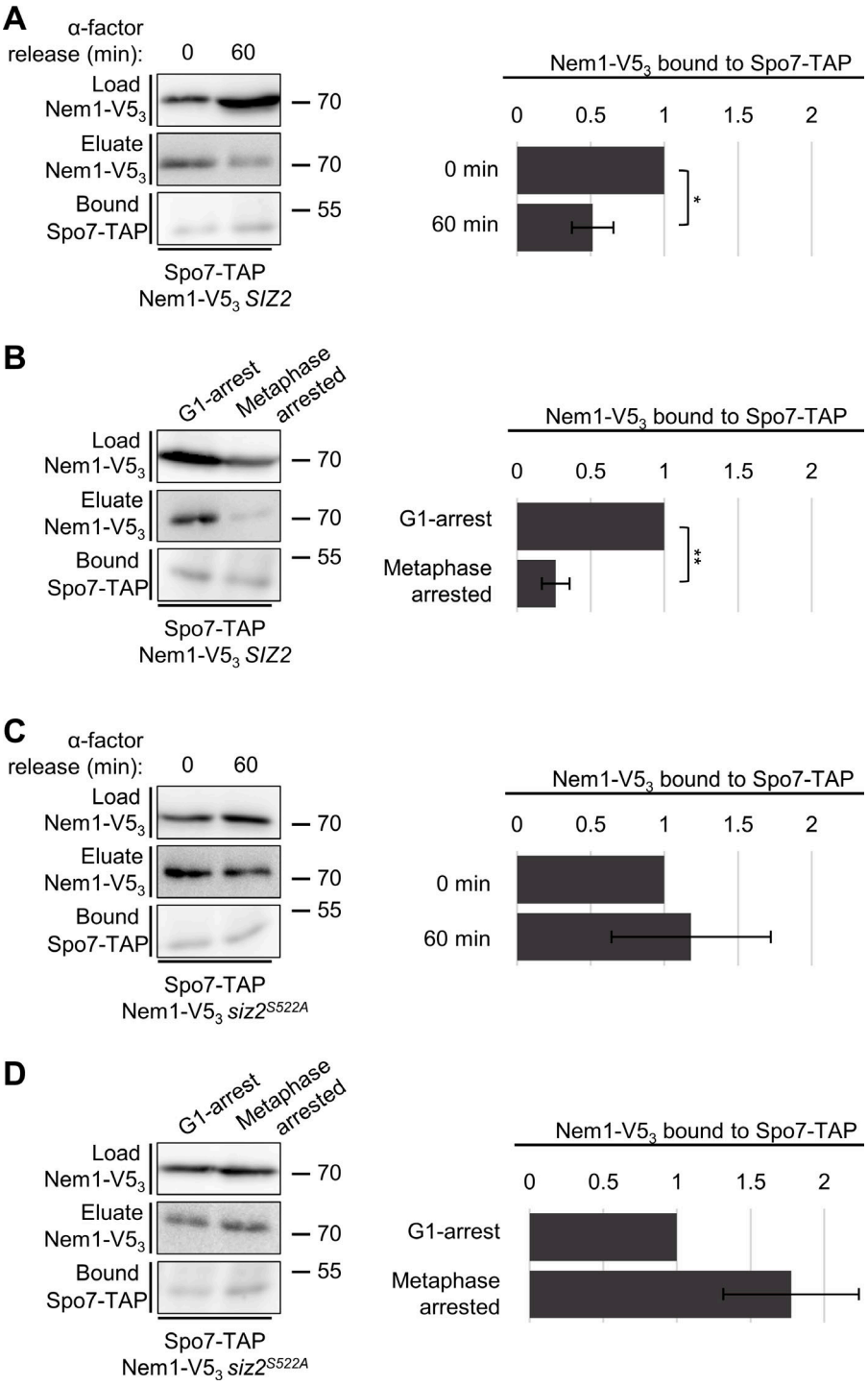

Figure 9. **Mitotic SUMOylation events reduce interactions between Spo7 and Nem1. (A and C)** WT (*SIZ2*) and *siz2*^{S522A} mutant cells, each expressing *SPO7-TAP* and *NEM1-V5*$_3$, were arrested in G1-phase with α-factor (0 min) and then released from arrest and allowed to proceed into mitosis (60 min after release). Spo7-Tap was affinity-purified and bound Nem1-V5$_3$ was examined at both time points as described in the Fig. 8 legend. **(B and D)** Results of the same purification and analysis procedures used to analyze Spo7-TAP-bound Nem1-V5$_3$ in WT (*SIZ2*) and *siz2*^{S522A} cells (each containing the *MET3pr-HA*$_3$*-CDC20* cassette) and arrested in G1-phase with α-factor or in metaphase by the depletion of Cdc20 (2 h after methionine addition). Adjacent bar graphs in each panel show quantification of the average relative ratio of Nem1-V5$_3$ bound (Eluate) to purified Spo7-TAP (Bound) from three affinity purification experiments (see Fig. 8 legend and Materials and methods). Mass markers are shown in kilodaltons. Error bars are SD, and p values were determined using a Student's paired *t* test. *p ≤ 0.05, **p ≤ 0.01. Source data are available for this figure: SourceData F9.

directed INM SUMOylation in interphase cells. Our data also indicate that deSUMOylation of the INM targets is required for cessation of NE expansion that would occur as cells exit mitosis and enter G1-phase. This conclusion is supported by the observation that *ulp1*$^{KE/YH}$ mutant cells, which contain elevated levels of NE-associated SUMO conjugates throughout the cell cycle (Ptak et al., 2021; Fig. 3 A), show increased nuclear surface area at all cell cycle stages (Fig. 3 C).

Our observations suggest that SUMOylation increases INM PA levels by inhibiting the association of Pah1 with the INM. This is supported by functional interactions of Siz2 and Ulp1 with Pah1 and regulators of its activity (Fig. 7) as well as the Siz2-dependent mitotic reduction in binding of Pah1 to the Spo7 membrane protein (Figs. 8 and 10). Previously, membrane association of Pah1 has been linked to its phosphorylation state (Choi et al., 2012; Choi et al., 2011; O'Hara et al., 2006). Specifically, the phosphorylation of Pah1 by multiple kinases appears to reduce membrane binding and PA phosphatase activity, while the Spo7/Nem1 phosphatase complex supports membrane binding and dephosphorylation of Pah1 resulting

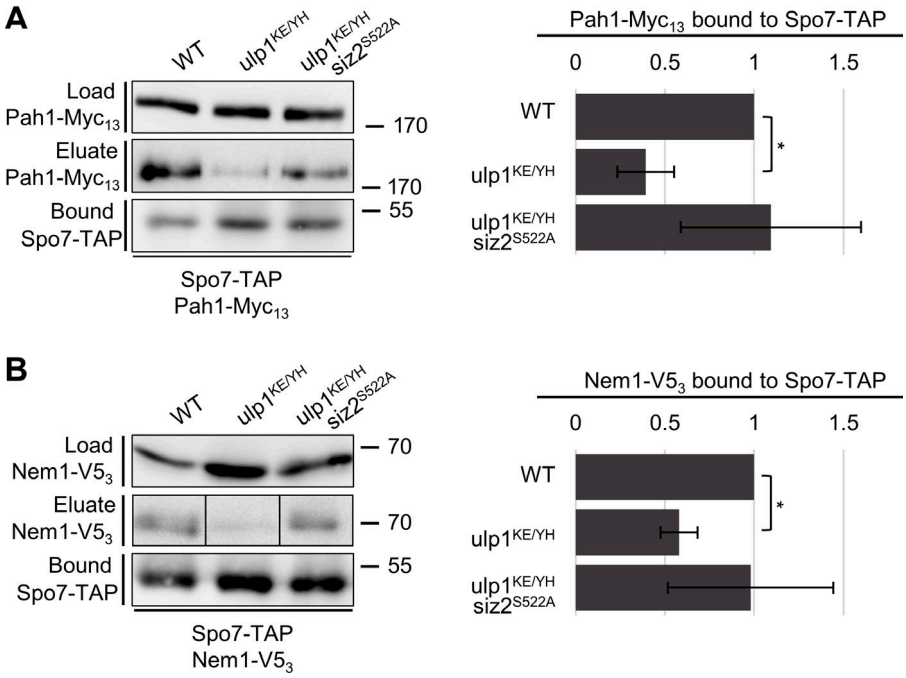

Figure 10. **Siz2-mediated SUMOylation events reduce Spo7 interactions with Pah1 and Nem1. (A and B)** WT, *ulp1*$^{KE/YH}$, and *ulp1*$^{KE/YH}$ *siz2*^{S522A} mutant cells producing Spo7-TAP and either Pah1-Myc_{13} (A) or Nem1-$V5_3$ (B) were harvested from asynchronous cultures and lysed. Spo7-Tap affinity purification and analysis of bound Pah1-Myc_{13} or Nem1-$V5_3$ were performed as outlined the Fig. 8 legend. Mass markers are shown in kilodaltons. All *ulp1*$^{KE/YH}$ mutant genes also encode a C-terminal GFP tag. Note that images shown in B, middle row, were derived from the same Western blot. Black lines indicate that intervening lanes have been spliced out. Quantification of affinity purification experiments is shown in the adjacent bar graphs and was performed as described in Fig. 8 with data representing three separate affinity purification experiments. Error bars are SD. Asterisks indicate a significant difference relative to WT as determined using a Student's paired *t* test. *p ≤ 0.05. Source data are available for this figure: SourceData F10.

in dephosphorylation of PA to DAG (Karanasios et al., 2010; Santos-Rosa et al., 2005; Siniossoglou et al., 1998; Su et al., 2014). During mitosis, phosphorylation of Pah1 by Cdk1 is proposed to reduce Pah1 membrane association and activity (Choi et al., 2011; O'Hara et al., 2006; Santos-Rosa et al., 2005). Consistent with this model, in mitotic cells, we detected a reduction in the association of Pah1 with the Spo7 membrane protein and Spo7 binding to Nem1 (Figs. 8 and 9). Both of these events are predicted to increase PA and decrease DAG levels and are in keeping with our observations (Figs. 4 and S3). Strikingly, the disassembly of these complexes during mitosis is dependent on Siz2 recruitment to the INM. Cells that do not target Siz2 to the INM (*siz2*^{S522A}) accumulated the Spo7/Nem1 complex and the associated Pah1 (Figs. 8 and 9), leading to decreased levels of PA (Fig. 4) and increased DAG (Fig. S3, D and E). Of note, despite increased Pah1 bound to the Spo7/Nem1 complex in *siz2*^{S522A} mutant cells, we did not detect an appreciable reduction in the mitotic phosphorylation state of Pah1, as might be predicted by this interaction (Fig. S3 H). It is possible our Western blot analysis of *siz2*^{S522A} mutant cells lacked the sensitivity to detect a reduction in Pah1 phosphorylation in this mutant. Thus, while our results establish a role for Siz2-mediated SUMOylation in inhibiting the membrane association of Pah1, how SUMOylation functions in concert with Pah1 phosphorylation to regulate Pah1 activity at the membrane remains to be determined.

Several observations led us to conclude that mitotic Siz2-mediated SUMOylation events driving Spo7/Nem1 dissociation and Pah1 inactivation occur at the INM. Siz2 is constitutively nuclear, and its mitotic phosphorylation induces its relocalization to the INM where it binds to and SUMOylates Scs2 and additional proteins, including, for example, the INM-associated telomere anchoring protein Sir4 (Ptak et al., 2021). Sir4 SUMOylation, however, while required for telomere association with the INM, is not required for NE expansion (Fig. S5). Beyond Scs2, other INM targets of Siz2-mediated SUMOylation that may contribute to inhibiting Pah1 and supporting NE accumulation of PA remain to be determined. Examining obvious potential targets such as Pah1, Spo7, and Nem1, each of which is found at the INM (Fig. S4 A; Romanauska and Köhler, 2018), has failed to detect their SUMOylation. Notably, however, the mammalian counterpart of Pah1, Lipin-1, is SUMOylated (Liu and Gerace, 2009). A likely alternative scenario is that a yet unidentified SUMO conjugate(s) binds Pah1, Spo7, and/or Nem1 and disrupts their interactions at the INM. Such SUMO conjugates are anticipated to be among the previously detected SUMO conjugates associated with the INM during mitosis (Ptak et al., 2021).

Other potential targets of SUMOylation that could increase PA levels in the INM might be found in pathways responsible for the production of PA, and whose increased activity could work in tandem with the inhibition of Pah1. Potential targets may include proteins directly responsible for the production of PA, such as Dgk1 and Slc1 (see Kwiatek et al., 2020), or other factors that increase the production of PA precursors. Moreover, we envisage that mitotic SUMOylation may also impact the function of other INM proteins that contribute to regulating lipid synthesis. In keeping with this idea, recent studies have detected proteins at the INM that participate in lipid metabolism, including those that control phospholipid synthesis and lipid storage, leading to proposals of local membrane biogenesis at the INM (Barbosa et al., 2019; Haider et al., 2018; Romanauska and Köhler, 2018). These pathways may be further revealed by future studies that more broadly define the SUMO proteome of the mitotic INM.

One Siz2 target at the INM whose SUMOylation is required for NE expansion (see *scs2*^{KI80R} Fig. 3) is Scs2, and we speculate that it may play multiple roles in these events. First, Scs2 and its conjugated SUMO form a binding site for Siz2 at the INM, and as

such Scs2-SUMO is required for the SUMOylation of other INM proteins (Ptak et al., 2021) and downstream effects, including increased INM levels of PA. In addition, SUMO-mediated regulation of other established functions of Scs2 in membrane biogenesis may also contribute to NE membrane expansion. As a member of the VAP protein family, Scs2 binds FFAT (Phenylalanine-Phenylalanine in an Acidic Tract) motifs present in various proteins, including several that regulate phospholipid metabolism (Brickner and Walter, 2004; Freyre et al., 2019; Manford et al., 2012). For example, Scs2 binds the transcriptional repressor Opi1 (Brickner and Walter, 2004; Loewen et al., 2003). It has been proposed that Scs2 sequesters Opi1 at the NE/ER membrane away from UAS_{INO}-containing phospholipid synthesizing genes, thus relieving transcriptional repression and promoting phospholipid synthesis (Brickner and Walter, 2004; Loewen et al., 2004; Loewen et al., 2003; Wilson et al., 2011). As Scs2 supports Opi1 binding to PA (Loewen et al., 2004), elevated levels of PA at the INM are also predicted to sequester Opi1 and support gene expression events that contribute to NE expansion. Thus, we envisage that mitotic-SUMOylation of INM Scs2 likely reflects a location-specific trigger for Scs2 functions in lipid biogenesis.

In summary, we demonstrate that a previously identified temporal increase in SUMOylation along the INM during mitosis couples the re-establishment of NE-chromatin interactions (Ptak et al., 2021) with NE membrane growth (this work). The mitotic burst in SUMOylation mediated by Siz2 restores binding of subtelomeric chromatin to the INM, the association of activated genes with the nuclear pore complexes, and, as we show here, increased NE membrane production. How each of these various events is coordinated by SUMOylation remains to be fully determined, and we expect further mechanistic insights will come from a broader annotation of mitotic Siz2 SUMOylation targets. Such analysis is also likely to reveal additional processes impacted by mitotic SUMOylation and potential functional links between these pathways. Finally, it is also important to consider that SUMO regulation of these pathways may not be limited to periods of mitosis. While trigged by mitotic phosphorylation and the redistribution of Siz2, SUMOylation may also function to regulate pathways outside of mitosis if alternative conditions induce a recruitment of Siz2 to the NE membrane or subdomains within. Such a mechanism seems reasonable as we have observed that tethering Siz2 to the INM at times outside of mitosis induces NE membrane expansion (Fig. 2). Notably, an increase in PA levels is detected in the region of the NE membrane adjacent to defective NPCs (Thaller et al., 2021), where membrane remodeling leads to the formation of NE herniations. It will be of interest to examine the role of Siz2-mediated SUMOylation in supporting other reported NE membrane remodeling processes, including nuclear pore complex formation.

Materials and methods

Yeast strains and plasmids

Yeast strains are listed in Table S1. All strains derive from S288C-based backgrounds, BY4741 or BY4742. Cells were grown in YPD medium (1% yeast extract, 2% bactopeptone, and 2% glucose), or a synthetic medium (SC) lacking the appropriate amino acid(s) (per l: 1.7 g yeast nitrogen base, 5 g ammonium acetate, 1.7 g amino acid dropout powder, and 2% glucose). Unless indicated otherwise, cell cultures were initially incubated overnight at room temperature (RT) with agitation. The following day, cultures were diluted into fresh medium to an OD_{600} = 0.1 and then incubated at 30°C for at least two generations prior to further use.

Yeast transformations were performed using a lithium acetate/polyethylene glycol method (Gietz and Woods, 2002). Yeast strains producing protein fusions, or strains in which a marker was switched, were generated by directed integration of a DNA cassette at a specific locus using a plasmid/PCR-based one-step method for gene modification (Longtine et al., 1998). PCR reactions used to generate DNA cassettes encoding the $V5_3$ or Myc_{13} epitope tags employed the plasmids pTM1198 (Lapetina et al., 2017) and pFA6a-13Myc-kanMX6 (Longtine et al., 1998), respectively, as a template. Strains carrying mutant *SIZ2*, *SCS2*, *ULP1*, or *GFP-SIZ2* alleles or *SUR4-mCherry* were derived from strains described in Ptak et al. (2021). Strains producing Pus1-GFP or a TAP-tagged protein fusion were derived from the corresponding strain found in the yeast GFP (Huh et al., 2003) or yeast TAP tag (Ghaemmaghami et al., 2003) library. Strains lacking *DGK1* and *SPO7* were derived from the corresponding strain found in the haploid Matα yeast deletion library (Invitrogen). *CDC20* shutoff strains were derived from a strain in which a DNA cassette, consisting of *KANMX-MET3pr-HA$_3$* that was generated by PCR using the plasmid pTM1406 (Makio et al., 2009), was integrated at the 5′ end of the *CDC20* start codon. The *KANMX* marker was then switched with *HPHMX* producing the *HPH-MET3pr-HA$_3$-CDC20* allele. Strains producing Siz2-GFP_{1-10} were generated as described in Smoyer et al. (2016), using the *pFA6-link-yGFP$_{1-10}$-CaURA3MX* (pSJ1256) plasmid. Strains producing GFP_{1-10}-Spo7 or GFP_{1-10}-Nem1 were also generated as described in Smoyer et al. (2016), using the *pFA6-NATMX-CDC42pr-yGFP$_{1-10}$* (pS1643) plasmid. Strains bearing multiple gene modifications were derived by crossing relevant strains followed by sporulation, dissection, and selection. Strains bearing multiple gene modifications that also lack *SPO7* were produced by integrating a PCR-amplified *spo7Δ* knockout cassette into the appropriate strain. Genomic DNA from the *spo7Δ::KANMX* Matα yeast deletion library strain was used as a template in the PCR.

Plasmids encoding GFP_{11}-mCherry-Scs2TM (pSJ1568; Smoyer et al., 2016), mCherry-Scs2TM-GFP_{11} (pSJ1602; Smoyer et al., 2016), siz2^{RING}-GFP_{1-10} (*pRS316-CUP1pr-siz2^{RING}-GFP$_{1-10}$*; this study), GFP_{11}-Scs2TM (*pGFP$_{11}$-SCS2TM*; this study), Scs2TM-GFP_{11} (*pGFP$_{11}$-Scs2TM*; this study), NLS-PA-mCherry (Romanauska and Köhler, 2018; *pRS315-CYC1prom-NUP60(1-24)-OPI1Q2-mCh*), PA-mCherry (Romanauska and Köhler, 2018; *pRS316-CYC1prom-OPI1Q2-mCh*), NLS-DAG-mCherry (Romanauska and Köhler, 2018; *pRS316-CYC1prom-C1a+C1b-mCh*), Pah1-PrA (Santos-Rosa et al., 2005, *YCplac111-PAH1-PtA*), or pah1^{7A}-PrA (O'Hara et al., 2006, *YCplac111-PAH1-7P-PtA*) were transformed into the indicated strains. To make *pGFP$_{11}$-SCS2TM*, the *NOP1pr-GFP$_{11}$-mCherry-SCS2TM* insert was excised from pSJ1568 (Smoyer et al., 2016)

using the EagI/NheI restriction enzyme sites and replaced by a *NOP1pr-GFP$_{11}$-SCS2TM* PCR cassette bounded by the EagI/NheI restriction sites. To make *pSCS2TM-GFP$_{11}$*, the *NOP1pr-mCherry* insert bounded by the EagI/NheI was excised from pSJ1602 (Smoyer et al., 2016) using the EagI/NheI restriction enzyme sites and replaced by a *NOP1pr* PCR cassette bounded by the EagI/NheI restriction sites. To make *pRS316-CUP1pr-siz2^{RING}-GFP$_{1-10}$*, 500 bp of the *CUP1* 5′UTR was synthesized by PCR using genomic DNA derived from BY4741 cells, along with the oligonucleotides Cup1-prS-Sal and Cup1-prAS-Sph. *siz2^{RING}-GFP$_{1-10}$* was synthesized by PCR using genomic DNA from a strain expressing *siz2$^{C354A/H356A}$-GFP$_{1-10}$* from the *SIZ2* locus as the template DNA along with the oligonucleotides Siz2-ORF-S-SphI and ADH1-3UTR-AS. Amino acid residue substitutions used to produce siz2^{RING} (siz2$^{C354A/H356A}$) were based on sequence comparisons shown in Johnson and Gupta (2001). Each PCR product was then cloned into pRS316 (Sikorski and Hieter, 1989) using the indicated restriction enzyme sites. Oligonucleotides used to produce PCR cassettes employed in plasmid construction and gene integration are listed in Table S2.

α-Factor arrest release assay

All strains used in α-factor arrest release assays were *MATa bar1Δ*. Cultures were incubated overnight at RT, diluted to an OD_{600} = 0.1 using fresh media, and then grown for ∼2.5 h at 30°C prior to the addition of α-factor (T6901; Sigma-Aldrich) to a final concentration of 10 ng/ml for cultures grown in YPD medium, and 20 ng/ml for cultures grown in SC medium. Cultures were then grown at 30°C for an additional ∼2 h to induce G1-phase arrest wherein >90% of the cells exhibit a mating projection. Aliquots of cells collected upon G1 arrest represent the 0 min time point. Arrested cells were then pelleted, washed once with water, and resuspended in fresh medium to a final OD_{600} = 0.6, thereby removing the α-factor. Cultures were then grown at 30°C, and aliquots were collected at the indicated time points for analysis by Western blotting, co-affinity purification, or epifluorescence microscopy.

Cdc20 shutoff assay

All strains used for metaphase arrest carried the *MET3pr-HA$_3$-CDC20* allele. Overnight cultures, grown in SC-Met medium at RT, were diluted to an OD_{600} = 0.1 in fresh SC-Met medium and were grown for two generations at 30°C prior to the addition of methionine to a final concentration of 20 µg/ml. Cultures were then incubated at 30°C for an additional 2 h to induce metaphase arrest. Arrest was confirmed microscopically wherein the majority of cells (>80%) appeared large-budded. Cells were collected for analysis by Western blotting, co-affinity purification, or epifluorescence microscopy.

Western blotting

Cell culture aliquots, equivalent to an OD_{600} = 1 of cells, were centrifuged and the resulting pellet was resuspended in 50 µl of 2× SDS-PAGE sample buffer. Samples were then heated at 65°C for 15 min, followed by sonication (Branson Sonifier 250; 10 pulses at 20% power) and subsequent centrifugation to remove cellular debris. These cell lysate samples were then loaded onto and ran through an 8% SDS-PAGE gel, followed by protein transfer from the gel onto a nitrocellulose membrane. Following the transfer, membranes were incubated for at least 1 h at RT in blocking buffer (PBS containing 0.1% Tween-20 [PBST] and 5% skim milk powder [SMP]). Membranes were then incubated in fresh PBST-SMP supplemented with primary antibody overnight at 4°C. Membranes were then washed three times with PBST for 15 min, followed by incubation in fresh PBST-SMP supplemented with a secondary antibody-HRP conjugate, for at least 1 h at RT. Membranes were then washed three times with PBST for 15 min, and proteins were subsequently visualized by chemiluminescence (32209; Pierce) using an ImageQuant LAS 4000 (GE) imaging system. All Western blot images were rendered using Image J software (National Institutes of Health). Western blots shown in Fig. 2 E were carried out as described above except that an Alexa Fluor 647–based secondary antibody was used. After washing, blots were air dried for ∼30 min prior to being imaged using a Typhoon FLA 9500 laser scanner at 600 V and 100 µm pixel size.

Primary antibodies used included rabbit polyclonal anti-Smt3 (Wozniak lab), mouse monoclonal anti-V5 (ab27671; AbCam), mouse monoclonal anti-Myc (11667149001; Roche), rabbit polyclonal anti-Clb2 (sc-9071; Santa Cruz), rabbit polyclonal anti-PrA (used to probe Spo7-TAP, Pah1-PrA and pah1^{7A}-PrA; P3775; Sigma-Aldrich), and rabbit polyclonal anti-Gsp1 (Wozniak lab). Secondary antibodies used included goat anti-rabbit IgG (H+L)-HRP conjugate (170-6515; BioRad), goat anti-mouse IgG (H+L)-HRP conjugate (170-6516; BioRad), and Alexa Fluor 647 F(ab')2-Goat anti-Rabbit IgG (H+L) Cross-Adsorbed (A21246; Thermo Fisher Scientific). Antibodies were all used at a 1:10,000 dilution.

Co-affinity purification

All co-affinity purifications employed strains producing a Spo7-TAP fusion protein and employed a procedure derived from that previously described in Van De Vosse et al. (2013).

For experiments coupling α-factor arrest release with co-affinity purification, a 50 ml YPD culture, grown overnight at RT, was diluted into 2 L of fresh YPD medium to an OD_{600} = 0.1. Cultures were then incubated at 30°C to an OD_{600} = 0.4. α-Factor was then added to a final concentration of 10 ng/ml, followed by incubation at 30°C for an additional 2.25 h to induce G1 phase arrest. The culture was then split into two 1-L aliquots. One aliquot was treated as described below to make "noodles" and was defined as the 0 min sample. Cells from the other aliquot were pelleted by centrifugation, washed once using 25 ml cold double-distilled water (ddH_2O), pelleted again, and then resuspended in 1 L of fresh YPD medium and incubated at 30°C for 60 min. Cells were then collected by centrifugation to make noodles (see below). This was defined as the 60-min sample.

For experiments coupling α-factor arrest (G1-arrest) and metaphase arrest with co-affinity purification, a 50 ml SC-Met culture, grown overnight at RT, was diluted into fresh SC-Met medium to generate two separate 1-L cultures, each with an OD_{600} = 0.1. The resulting cultures were then incubated at 30°C to an OD_{600} = 0.4. α-Factor was then added to one culture to a final concentration of 20 ng/ml, followed by incubation at 30°C for an additional 2.25 h to induce G1 phase arrest. Methionine was added to the other culture to a final concentration of 20 µg/ml

followed by incubation at 30°C for an additional 2 h to induce metaphase arrest. In both cases, cells were pelleted after arrest and washed once using 25 ml cold ddH_2O. Cells were then collected by centrifugation to make noodles (see below).

Each final cell pellet was transferred, using a spatula, to a 10-ml syringe and the cells were then extruded through the syringe directly into a 50-ml falcon tube containing liquid nitrogen for flash freezing. The liquid nitrogen was then removed and the resulting cell noodles were stored at −80°C.

Frozen cell noodles were then lysed by ball mill grinding (PM100; Reitch; 8 × 90 s at 450 rpm with cooling in liquid nitrogen between rounds). The resulting cell powder was collected into a liquid nitrogen–cooled 50-ml falcon tube and then stored at −80°C. 1 g of cell powder was subsequently resuspended in 2 ml of cold IP buffer (2 mM $MgCl_2$, 20 mM HEPES-KOH, pH 7.4, 0.1% Tween-20, 110 mM KOAc, antifoam-B emulsion at 1:5,000 dilution, and one complete EDTA-free protease inhibitor pellet [05056489001; Roche]/50 ml buffer). This suspension was then incubated on ice for 30 min, with vortexing every 5 min, and the resulting lysate was cleared by centrifugation at 1,500 × *g* for 10 min at 4°C. 25 µl of the clarified lysate, representing the load, was added to 1 ml of ddH_2O, followed by TCA precipitation. The resulting pellet was resuspended in 75 µl of 2× SDS-PAGE sample buffer. 3 mg of IgG-conjugated magnetic beads (see below for bead preparation) in 100 µl of IP buffer was added to the remaining clarified cell lysate and the mixture was incubated for 1 h at 4°C with rotation. Note, all remaining coaffinity purification steps were carried out at 4°C. Beads were collected using a magnet and washed 10 times with 1 ml of IP buffer. Proteins bound to beads were eluted using 0.5 ml IP buffer containing incrementally increasing concentrations of $MgCl_2$ (0.05, 0.5, and 2 M) followed by a final elution using 0.5 ml of 0.5 M acetic acid to release the TAP fusion protein from the beads (Bound). To the 500 µl eluate fractions, 500 µl of ddH_20 was added followed by TCA precipitation. The resulting pellets were resuspended in 75 µl of 2× SDS-PAGE sample buffer, and equal amounts from each eluate sample were combined prior to Western blot analysis.

For bead preparation, IgG was conjugated to magnetic beads as previously described (Alber et al., 2007; Van De Vosse et al., 2013). 10 mg of rabbit IgG (Sigma-Aldrich) was dissolved in 2 ml of Na-phosphate buffer (0.1 M $NaPO_4$, pH 7.4) for 10 min, with rotation, at RT. The solution was clarified by centrifugation at 14,000 rpm for 10 min at 4°C. To this clarified solution, 2 ml Na-phosphate buffer and 1.33 ml of 3 M ammonium sulfate pH 7.5 was added. 60 mg of Epoxy M-270 Dynabeads, which had been washed and equilibrated with the Na-phosphate buffer, was then added to the IgG solution and the suspension was incubated at 30°C for 20 h with rotation to facilitate IgG conjugation to the magnetic beads. Following incubation, the IgG-conjugated beads were sequentially washed once with 1 ml 100 mM glycine, pH 2.5, once with 1 ml 10 mM Tris, pH 8.8, once with 1 ml 100 mM triethylamine, pH 6.0, four times with 1 ml PBS for 5 min per wash, once with 1 ml PBS + 0.5% Triton X-100 for 5 min, and once with 1 ml PBS + 0.5% Triton X-100 for 15 min, followed by three washes with 1 ml PBS for 5 min per wash. Washed beads were then resuspended in 2 ml PBS + 0.02% sodium azide and stored at 4°C.

Anti-SUMO immunofluorescence

Anti-SUMO immunofluorescence was performed as described in Ptak et al. (2021). To 5 ml of a mid–log phase culture (~OD_{600} = 0.8), 0.6 ml of 10× phosphate buffer (1 M KH_2PO_4, 370 mM KOH, 0.5 mM $MgCl_2$) and 0.8 ml of 37% formaldehyde were added followed by incubation at 30°C for 30 min with rotation. Cells were then pelleted and washed twice with 1× phosphate buffer. The final pellets were resuspended in 100 ml of sorbitol-citrate buffer (100 mM K_2PO_4, 3.6 mM citric acid, 1.2 M sorbitol, 0.5 mM $MgCl_2$), DTT was added to a final concentration of 1 mM, and the mixture was incubated for 1 min at RT. Cells were pelleted, then resuspended in 100 ml of sorbitol-citrate buffer supplemented with 2 mg/ml 20T zymolyase (BioShop) and incubated at 30°C for 20 min. Cells were then pelleted, washed twice with 1 ml sorbitol-citrate buffer, and the final cell pellet was resuspended in 50 ml of sorbitol-citrate buffer. 20 ml of the cell suspension was pipetted onto a multiwell slide coated with 0.1% poly-*L*-lysine followed by incubation of the slide at RT in a covered box lined with damp paper towels for 30 min. All subsequent incubations and washes were carried out at RT in the same box with ~20 µl of each solution. Steps included (1) one PBST wash, (2) one wash with 0.1% Triton X-100 in PBS for 10 min, (3) two washes with PBST, (4) blocking step with 1% BSA in PBST for 10 min, (4) 1% BSA in PBST supplemented with a rabbit polyclonal anti-SUMO antibody (Wozniak lab) at a 1:500 dilution with a 1-h incubation, (5) ten washes with 0.1% BSA in PBST, (6) one addition of 1% BSA PBST supplemented with Alexa Fluor 488 donkey anti-rabbit IgG antibody (A11055; Life Technologies) at a 1:200 dilution with a 1-h incubation, and (6) ten washes with 0.1% BSA in PBST. After the final wash, ~3 µl of DAPI-Fluoromount-G (0100-20; SouthernBiotech) was added to each well, and a coverslip was placed over the slide. Cells were then analyzed by epifluorescence imaging.

Epifluorescence microscopy

Epifluorescence images were acquired on a DeltaVision Elite imaging system (GE Healthcare Life Sciences) with a 60×/1.42 NA oil, Plan Apo N objective (Olympus). Images were collected using the SoftWoRx software (version 6.5.2, GE Healthcare Life Sciences) as 15 × 0.2 µm z-stacks or, in the case of images used for calculating nuclear surface area, as 40 × 0.2 µm z-stacks. All cultures used for live cell imaging were grown to mid–log phase at 30°C, except for GFP-Siz2 strains which were incubated at RT. Cells were then pelleted by centrifugation, washed once with ddH_2O, and resuspended in an SC medium. 1.5 µl of this cell suspension was then spotted onto a microscope slide and imaged at RT.

Image analysis

Images were rendered and analyzed using Image J (National Institutes of Health) software. Representative images used in figures and for quantification were treated using the unsharp mask filter (Radius [Sigma-Aldrich]: 2.0 pixels; Mask Weight: 0.8). The cell cycle stage of cells was assessed based on bud size and/or nuclear morphology. Specifically, G1-phase, unbudded cells, round nucleus; S-phase, small-budded cells, round nucleus away from budneck; and M-phase, large-budded cells, barbell-shaped nuclei.

For line scan quantifications, images from each channel were rendered in Image J as described above and converted to an 8-bit image. Then, the images were stacked into a single file. A line, 1.85 µm in length, was drawn through individual cell nuclei and the fluorescence intensity along the line was quantified for each channel. Each line segment was drawn through an equatorial optical section, such that the line drawn was centered upon the DAPI or Pus1-GFP signal or the line passed through two points of the Sur4-mCherry signal along the NE, avoiding the nucleolus.

The nuclear surface area was quantified using Imaris software that generated a three-dimensional reconstruction of nuclei using the nucleoplasmic Pus1-GFP fluorescent signal (Surface detail 0.2 µm, thresholding: background subtraction 0.813 µm). Images were initially acquired on the DeltaVision microscope as 40 × 0.2 µm z-stacks, followed by deconvolution using the iterative 15-cycle conservative ratio in the softWoRx program (version 6.5.2, GE Healthcare Life Sciences) prior to analysis using Imaris software. In the case of cells in late mitosis, the nuclear surface area bounded by the membrane bridge between mother and daughter nuclei was approximated by measuring bridge length and assuming the bridge to be a cylinder with a radius of 58 nm (Yamaguchi et al., 2011). The surface area of the mother nucleus, daughter nucleus, and membrane bridge were then added to derive the total nuclear surface area.

Protein quantification

Affinity purification of Spo7-TAP, from WT and/or mutant strains grown under the same conditions, was carried out in parallel. Levels of proteins copurifying with Spo7-TAP from these strains were compared as previously described in Lapetina et al. (2017). Fractions from a given co-affinity purification were run through the same SDS-PAGE gel and analyzed simultaneously by Western blotting. Signal intensities, corrected for background, of the copurifying protein in the eluate (E_I) as well as that of Spo7-TAP bound to the beads were quantified using ImageQuant software (GE). The signal intensity of the copurifying protein was normalized to the amount of Spo7-TAP bound to the beads by calculating the ratio between E_I and the signal intensity of Spo7-TAP (E_I/Bound = E_{IB}). All E_{IB} values were then graphed as a ratio relative to that observed for WT, or in the case of α-factor arrest/release experiments as a ratio relative to that observed for the 0 min time point, or in the case of cell cycle arrest as a ratio relative to that observed under G1-arrest.

Statistical analysis

All graphs were generated using Excel. Data distribution was assumed to be normal but was not formally tested. The average of at least three replicates is shown for all surface area analyses (n = 50 cells/replicate/cell cycle stage) with error bars representing SD. Significance was assessed relative to the indicated counterpart using a two-tailed Student's t test (*$p \le 0.05$, **$p \le 0.01$, ***$p \le 0.001$). The average of three replicates is shown for all co-affinity purification experiments with error bars representing SD. Significance was determined using a paired Student's t test (*$p \le 0.05$, **$p \le 0.01$). Signal variance for GFP-Siz2, Sur4-mCherry, SUMO, DAPI, the NLS-PA sensor, and the NLS-DAG sensor is presented as error bars showing SD (n = 25 cells/cell cycle stage).

Online supplemental material

Fig. S1 shows cell cycle SUMOylation profiles between WT and *siz2*^{S522A} mutant cells, as well as Siz2 localization in metaphase-arrested cells. Fig. S2 shows Siz2 and siz2^{S522A} localization in *ulp1*$^{KE/YH}$ mutant cells. Fig. S3 shows cytoplasmic PA levels and DAG levels at the INM, as well as SUMOylation profiles in the presence of exogenously expressed *PAH1* and *pah1*^{7A} and the electrophoretic mobility of Pah1 in asynchronous and metaphase arrested WT and *siz2*^{S522A} mutant cells. Fig. S4 shows the INM localization of Spo7 and Nem1, the extraction efficiency of Spo7-TAP, and interactions between Spo7 and Ice2. Fig S5 shows the nuclear surface area of metaphase arrested WT, *siz2*^{S522A}, and *sir4*^{K1037R} cells. Table S1 shows the list of strains and genotypes. Table S2 lists oligonucleotides and sequences.

Data availability

All data are available in the published article and in the online supplemental material.

Acknowledgments

We thank members of the Aitchison, Montpetit, and Wozniak labs as well as Ed Hurt (Heidelberg University), Richard Rachubinski, and Richard Lehner (University of Alberta) for helpful discussions.

Funding for this work is supported by the Canadian Institutes of Health Research (MOP 106502 and PJT 180467) to R.W. Wozniak and the National Institutes of Health, USA (NCDIR: 2P41GM109824-06 and R01: 2R01GM112108-05 to J.D. Aitchison and R01GM124120 to B. Montpetit).

Author contributions: Conceptualization: N.O. Saik, C. Ptak, J.D. Aitchison, B. Monpetit, and R.W. Wozniak; Methodology: N.O. Saik and R.W. Wozniak; Investigation: N.O. Saik, C. Ptak, and S. Rehman; Validation: N.O. Saik and C. Ptak; Funding acquisition: R.W. Wozniak; Project administration: R.W. Wozniak; Visualization: N.O. Saik and R.W. Wozniak; Writing—original draft: N.O. Saik and R.W. Wozniak; Writing—review and editing: N.O. Saik, C. Ptak, J.D. Aitchison, B. Monpetit, and R.W. Wozniak.

Disclosures: The authors declare no competing interests exist.

Submitted: 24 August 2022
Revised: 24 March 2023
Accepted: 15 May 2023

References

Alber, F., S. Dokudovskaya, L.M. Veenhoff, W. Zhang, J. Kipper, D. Devos, A. Suprapto, O. Karni-Schmidt, R. Williams, B.T. Chait, et al. 2007. The molecular architecture of the nuclear pore complex. *Nature*. 450: 695–701. https://doi.org/10.1038/nature06405

Barbosa, A.D., K. Lim, M. Mari, J.R. Edgar, L. Gal, P. Sterk, B.J. Jenkins, A. Koulman, D.B. Savage, M. Schuldiner, et al. 2019. Compartmentalized synthesis of triacylglycerol at the inner nuclear membrane regulates nuclear organization. *Dev. Cell*. 50:755–766.e6. https://doi.org/10.1016/j.devcel.2019.07.009

Brachmann, C.B., A. Davies, G.J. Cost, E. Caputo, J. Li, P. Hieter, and J.D. Boeke. 1998. Designer deletion strains derived from Saccharomyces

cerevisiae S288C: a useful set of strains and plasmids for PCR-mediated gene disruption and other applications. *Yeast*. 14(2):115–132. https://doi.org/10.1002/(SICI)1097-0061(19980130)14:2<115::AID-YEA204>3.0.CO;2-2

Brickner, J.H., and P. Walter. 2004. Gene recruitment of the activated INO1 locus to the nuclear membrane. *PLoS Biol.* 2:e342. https://doi.org/10.1371/journal.pbio.0020342

Campbell, J.L., A. Lorenz, K.L. Witkin, T. Hays, J. Loidl, and O. Cohen-Fix. 2006. Yeast nuclear envelope subdomains with distinct abilities to resist membrane expansion. *Mol. Biol. Cell*. 17:1768–1778. https://doi.org/10.1091/mbc.e05-09-0839

Carman, G.M., and G.S. Han. 2011. Regulation of phospholipid synthesis in the yeast *Saccharomyces cerevisiae*. *Annu. Rev. Biochem.* 80:859–883. https://doi.org/10.1146/annurev-biochem-060409-092229

Chandra, S., P.J. Mannino, D.J. Thaller, N.R. Ader, M.C. King, T.J. Melia, and C.P. Lusk. 2021. Atg39 selectively captures inner nuclear membrane into lumenal vesicles for delivery to the autophagosome. *J. Cell Biol.* 220: e202103030. https://doi.org/10.1083/jcb.202103030

Choi, H.S., W.M. Su, G.S. Han, D. Plote, Z. Xu, and G.M. Carman. 2012. Pho85p-Pho80p phosphorylation of yeast Pah1p phosphatidate phosphatase regulates its activity, location, abundance, and function in lipid metabolism. *J. Biol. Chem.* 287:11290–11301. https://doi.org/10.1074/jbc.M112.346023

Choi, H.S., W.M. Su, J.M. Morgan, G.S. Han, Z. Xu, E. Karanasios, S. Siniossoglou, and G.M. Carman. 2011. Phosphorylation of phosphatidate phosphatase regulates its membrane association and physiological functions in *Saccharomyces cerevisiae*: Identification of SER(602), THR(723), and SER(744) as the sites phosphorylated by CDC28 (CDK1)-encoded cyclin-dependent kinase. *J. Biol. Chem.* 286:1486–1498. https://doi.org/10.1074/jbc.M110.155598

Dubots, E., S. Cottier, M.P. Péli-Gulli, M. Jaquenoud, S. Bontron, R. Schneiter, and C. De Virgilio. 2014. TORC1 regulates Pah1 phosphatidate phosphatase activity via the Nem1/Spo7 protein phosphatase complex. *PLoS One*. 9:e104194. https://doi.org/10.1371/journal.pone.0104194

Foo, S., A. Cazenave-Gassiot, M.R. Wenk, and S. Oliferenko. 2023. Diacylglycerol at the inner nuclear membrane fuels nuclear envelope expansion in closed mitosis. *J. Cell Sci.* 136:1–14. https://doi.org/10.1242/jcs.260568

Freyre, C.A.C., P.C. Rauher, C.S. Ejsing, and R.W. Klemm. 2019. MIGA2 links mitochondria, the ER, and lipid droplets and promotes de novo lipogenesis in adipocytes. *Mol. Cell*. 76:811–825.e14. https://doi.org/10.1016/j.molcel.2019.09.011

Ghaemmaghami, S., W.K. Huh, K. Bower, R.W. Howson, A. Belle, N. Dephoure, E.K. O'Shea, and J.S. Weissman. 2003. Global analysis of protein expression in yeast. *Nature*. 425:737–741. https://doi.org/10.1038/nature02046

Gietz, R.D., and R.A. Woods. 2002. Transformation of yeast by lithium acetate/single-stranded carrier DNA/polyethylene glycol method. *Methods Enzymol.* 350:87–96. https://doi.org/10.1016/S0076-6879(02)50957-5

Grimsey, N., G.S. Han, L. O'Hara, J.J. Rochford, G.M. Carman, and S. Siniossoglou. 2008. Temporal and spatial regulation of the phosphatidate phosphatases lipin 1 and 2. *J. Biol. Chem.* 283:29166–29174. https://doi.org/10.1074/jbc.M804278200

Haider, A., Y.C. Wei, K. Lim, A.D. Barbosa, C.H. Liu, U. Weber, M. Mlodzik, K. Oras, S. Collier, M.M. Hussain, et al. 2018. PCYT1A regulates phosphatidylcholine homeostasis from the inner nuclear membrane in response to membrane stored curvature elastic stress. *Dev. Cell*. 45: 481–495.e8. https://doi.org/10.1016/j.devcel.2018.04.012

Han, G.S., L. O'Hara, G.M. Carman, and S. Siniossoglou. 2008. An unconventional diacylglycerol kinase that regulates phospholipid synthesis and nuclear membrane growth. *J. Biol. Chem.* 283:20433–20442. https://doi.org/10.1074/jbc.M802903200

Han, G.S., W.I. Wu, and G.M. Carman. 2006. The *Saccharomyces cerevisiae* Lipin homolog is a Mg^{2+}-dependent phosphatidate phosphatase enzyme. *J. Biol. Chem.* 281:9210–9218. https://doi.org/10.1074/jbc.M600425200

Harris, T.E., T.A. Huffman, A. Chi, J. Shabanowitz, D.F. Hunt, A. Kumar, and J.C. Lawrence Jr. 2007. Insulin controls subcellular localization and multisite phosphorylation of the phosphatidic acid phosphatase, lipin 1. *J. Biol. Chem.* 282:277–286. https://doi.org/10.1074/jbc.M609537200

Hassaninasab, A., G.S. Han, and G.M. Carman. 2017. Tips on the analysis of phosphatidic acid by the fluorometric coupled enzyme assay. *Anal. Biochem.* 526:69–70. https://doi.org/10.1016/j.ab.2017.03.020

Hetzer, M.W. 2010. The nuclear envelope. *Cold Spring Harb. Perspect. Biol.* 2(3):a000539. https://doi.org/10.1101/cshperspect.a000539

Huffman, T.A., I. Mothe-Satney, and J.C. Lawrence Jr. 2002. Insulin-stimulated phosphorylation of lipin mediated by the mammalian target of rapamycin. *Proc. Natl. Acad. Sci. USA*. 99:1047–1052. https://doi.org/10.1073/pnas.022634399

Huh, W.K., J.V. Falvo, L.C. Gerke, A.S. Carroll, R.W. Howson, J.S. Weissman, and E.K. O'Shea. 2003. Global analysis of protein localization in budding yeast. *Nature*. 425:686–691. https://doi.org/10.1038/nature02026

Jentsch, S., and I. Psakhye. 2013. Control of nuclear activities by substrate-selective and protein-group SUMOylation. *Annu. Rev. Genet.* 47:167–186. https://doi.org/10.1146/annurev-genet-111212-133453

Johnson, E.S., and A.A. Gupta. 2001. An E3-like factor that promotes SUMO conjugation to the yeast septins. *Cell*. 106:735–744. https://doi.org/10.1016/S0092-8674(01)00491-3

Karanasios, E., G.S. Han, Z. Xu, G.M. Carman, and S. Siniossoglou. 2010. A phosphorylation-regulated amphipathic helix controls the membrane translocation and function of the yeast phosphatidate phosphatase. *Proc. Natl. Acad. Sci. USA*. 107:17539–17544. https://doi.org/10.1073/pnas.1007974107

Kwiatek, J.M., G.S. Han, and G.M. Carman. 2020. Phosphatidate-mediated regulation of lipid synthesis at the nuclear/endoplasmic reticulum membrane. *Biochim. Biophys. Acta Mol. Cell Biol. Lipids*. 1865:158434. https://doi.org/10.1016/j.bbalip.2019.03.006

Lapetina, D.L., C. Ptak, U.K. Roesner, and R.W. Wozniak. 2017. Yeast silencing factor Sir4 and a subset of nucleoporins form a complex distinct from nuclear pore complexes. *J. Cell Biol.* 216:3145–3159. https://doi.org/10.1083/jcb.201609049

Lin, Y.P., and G.M. Carman. 1989. Purification and characterization of phosphatidate phosphatase from *Saccharomyces cerevisiae*. *J. Biol. Chem.* 264:8641–8645. https://doi.org/10.1016/s0021-9258(18)81840-3

Liu, G.H., and L. Gerace. 2009. Sumoylation regulates nuclear localization of lipin-1α in neuronal cells. *PLoS One*. 4:e7031. https://doi.org/10.1371/journal.pone.0007031

Loewen, C.J.R., M.L. Gazpar, S.A. Jesch, C. Delon, N.T. Ktistakis, S.A. Henry, and T.P. Levine. 2004. Phospholipid metabolism regulated by a transcription factor sensing phosphatidic acid. *Science*. 304:1644–1647. https://doi.org/10.1126/science.1096083

Loewen, C.J.R., A. Roy, and T.P. Levine. 2003. A conserved ER targeting motif in three families of lipid binding proteins and in Opi1p binds VAP. *EMBO J.* 22:2025–2035. https://doi.org/10.1093/emboj/cdg201

Longtine, M.S., A. McKenzie III, D.J. Demarini, N.G. Shah, A. Wach, A. Brachat, P. Philippsen, and J.R. Pringle. 1998. Additional modules for versatile and economical PCR-based gene deletion and modification in *Saccharomyces cerevisiae*. *Yeast*. 14:953–961. https://doi.org/10.1002/(SICI)1097-0061(199807)14:10<953:AID-YEA293>3.0.CO;2-U

Makio, T., L.H. Stanton, C.C. Lin, D.S. Goldfarb, K. Weis, and R.W. Wozniak. 2009. The nucleoporins Nup170p and Nup157p are essential for nuclear pore complex assembly. *J. Cell Biol.* 185:459–473. https://doi.org/10.1083/jcb.200810029

Manford, A.G., C.J. Stefan, H.L. Yuan, J.A. Macgurn, and S.D. Emr. 2012. ER-to-plasma membrane tethering proteins regulate cell signaling and ER morphology. *Dev. Cell*. 23:1129–1140. https://doi.org/10.1016/j.devcel.2012.11.004

Misteli, T. 2020. The self-organizing genome: Principles of genome architecture and function. *Cell*. 183:28–45. https://doi.org/10.1016/j.cell.2020.09.014

Moriuchi, T., and F. Hirose. 2021. SUMOylation of RepoMan during late telophase regulates dephosphorylation of lamin A. *J. Cell Sci.* 134:1–15. https://doi.org/10.1242/jcs.247171

Moriuchi, T., M. Kuroda, F. Kusumoto, T. Osumi, and F. Hirose. 2016. Lamin A reassembly at the end of mitosis is regulated by its SUMO-interacting motif. *Exp. Cell Res.* 342:83–94. https://doi.org/10.1016/j.yexcr.2016.02.016

O'Hara, L., G.S. Han, S. Peak-Chew, N. Grimsey, G.M. Carman, and S. Siniossoglou. 2006. Control of phospholipid synthesis by phosphorylation of the yeast lipin Pah1p/Smp2p Mg^{2+}-dependent phosphatidate phosphatase. *J. Biol. Chem.* 281:34537–34548. https://doi.org/10.1074/jbc.M606654200

Papagiannidis, D., P.W. Bircham, C. Lüchtenborg, O. Pajonk, G. Ruffini, B. Brügger, and S. Schuck. 2021. Ice2 promotes ER membrane biogenesis in yeast by inhibiting the conserved lipin phosphatase complex. *EMBO J.* 40:e107958. https://doi.org/10.15252/embj.2021107958

Pascual, F., A. Soto-Cardalda, and G.M. Carman. 2013. PAH1-encoded phosphatidate phosphatase plays a role in the growth phase- and inositol-mediated regulation of lipid synthesis in *Saccharomyces cerevisiae*. *J. Biol. Chem.* 288:35781–35792. https://doi.org/10.1074/jbc.M113.525766

Péterfy, M., J. Phan, P. Xu, and K. Reue. 2001. Lipodystrophy in the fld mouse results from mutation of a new gene encoding a nuclear protein, lipin. *Nat. Genet.* 27:121–124. https://doi.org/10.1038/83685

Peterson, T.R., S.S. Sengupta, T.E. Harris, A.E. Carmack, S.A. Kang, E. Balderas, D.A. Guertin, K.L. Madden, A.E. Carpenter, B.N. Finck, and D.M. Sabatini. 2011. mTOR complex 1 regulates lipin 1 localization to control the SREBP pathway. *Cell.* 146:408–420. https://doi.org/10.1016/j.cell.2011.06.034

Ptak, C., J.D. Aitchison, and R.W. Wozniak. 2014. The multifunctional nuclear pore complex: A platform for controlling gene expression. *Curr. Opin. Cell Biol.* 28:46–53. https://doi.org/10.1016/j.ceb.2014.02.001

Ptak, C., N.O. Saik, A. Premashankar, D.L. Lapetina, J.D. Aitchison, B. Montpetit, and R.W. Wozniak. 2021. Phosphorylation-dependent mitotic SUMOylation drives nuclear envelope-chromatin interactions. *J. Cell Biol.* 220:e202103036. https://doi.org/10.1083/jcb.202103036

Rodriguez Sawicki, L., K.A. Garcia, B. Corsico, and N. Scaglia. 2019. De novo lipogenesis at the mitotic exit is used for nuclear envelope reassembly/expansion. Implications for combined chemotherapy. *Cell Cycle.* 18:1646–1659. https://doi.org/10.1080/15384101.2019.1629792

Romanauska, A., and A. Köhler. 2018. The inner nuclear membrane is a metabolically active territory that generates nuclear lipid droplets. *Cell.* 174:700–715.e18. https://doi.org/10.1016/j.cell.2018.05.047

Santos-Rosa, H., J. Leung, N. Grimsey, S. Peak-Chew, and S. Siniossoglou. 2005. The yeast lipin Smp2 couples phospholipid biosynthesis to nuclear membrane growth. *EMBO J.* 24:1931–1941. https://doi.org/10.1038/sj.emboj.7600672

Scaglia, N., S. Tyekucheva, G. Zadra, C. Photopoulos, and M. Loda. 2014. De novo fatty acid synthesis at the mitotic exit is required to complete cellular division. *Cell Cycle.* 13:859–868. https://doi.org/10.4161/cc.27767

Sikorski, R.S., and P. Hieter. 1989. A system of shuttle vectors and yeast host strains designed for efficient manipulation of DNA in *Saccharomyces cerevisiae*. *Genetics.* 122:19–27. https://doi.org/10.1093/genetics/122.1.19

Siniossoglou, S., H. Santos-Rosa, J. Rappsilber, M. Mann, and E. Hurt. 1998. A novel complex of membrane proteins required for formation of a spherical nucleus. *EMBO J.* 17:6449–6464. https://doi.org/10.1093/emboj/17.22.6449

Smoyer, C.J., S.S. Katta, J.M. Gardner, L. Stoltz, S. McCroskey, W.D. Bradford, M. McClain, S.E. Smith, B.D. Slaughter, J.R. Unruh, and S.L. Jaspersen. 2016. Analysis of membrane proteins localizing to the inner nuclear envelope in living cells. *J. Cell Biol.* 215:575–590. https://doi.org/10.1083/jcb.201607043

Su, W.-M., G.-S. Han, and G.M. Carman. 2014. Yeast Nem1-Spo7 protein phosphatase activity on Pah1 phosphatidate phosphatase is specific for the Pho85-Pho80 protein kinase phosphorylation sites. *J. Biol. Chem.* 289(50):34699–34708. https://doi.org/10.1074/jbc.M114.614883

Thaller, D.J., D. Tong, C.J. Marklew, N.R. Ader, P.J. Mannino, S. Borah, M.C. King, B. Ciani, and C.P. Lusk. 2021. Direct binding of ESCRT protein Chm7 to phosphatidic acid-rich membranes at nuclear envelope herniations. *J. Cell Biol.* 220:e202004222. https://doi.org/10.1083/jcb.202004222

Van de Vosse, D.W., Y. Wan, D.L. Lapetina, W.M. Chen, J.H. Chiang, J.D. Aitchison, and R.W. Wozniak. 2013. A role for the nucleoporin Nup170p in chromatin structure and gene silencing. *Cell.* 152:969–983. https://doi.org/10.1016/j.cell.2013.01.049

Wang, R., A. Kamgoue, C. Normand, I. Léger-Silvestre, T. Mangeat, and O. Gadal. 2016. High resolution microscopy reveals the nuclear shape of budding yeast during cell cycle and in various biological states. *J. Cell Sci.* 129:4480–4495. https://doi.org/10.1242/jcs.188250

Webster, M.T., J.M. McCaffery, and O. Cohen-Fix. 2010. Vesicle trafficking maintains nuclear shape in *Saccharomyces cerevisiae* during membrane proliferation. *J. Cell Biol.* 191:1079–1088. https://doi.org/10.1083/jcb.201006083

Wilson, J.D., S.L. Thompson, and C. Barlowe. 2011. Yet1p-Yet3p interacts with Scs2p-Opi1p to regulate ER localization of the Opi1p repressor. *Mol. Biol. Cell.* 22:1430–1439. https://doi.org/10.1091/mbc.e10-07-0559

Witkin, K.L., Y. Chong, S. Shao, M.T. Webster, S. Lahiri, A.D. Walters, B. Lee, J.L.Y. Koh, W.A. Prinz, B.J. Andrews, and O. Cohen-Fix. 2012. The budding yeast nuclear envelope adjacent to the nucleolus serves as a membrane sink during mitotic delay. *Curr. Biol.* 22:1128–1133. https://doi.org/10.1016/j.cub.2012.04.022

Yamaguchi, M., Y. Namiki, H. Okada, Y. Mori, H. Furukawa, J. Wang, M. Ohkusu, and S. Kawamoto. 2011. Structome of *Saccharomyces cerevisiae* determined by freeze-substitution and serial ultrathin-sectioning electron microscopy. *J. Electron Microsc.* 60:321–335. https://doi.org/10.1093/jmicro/dfr052

Supplemental material

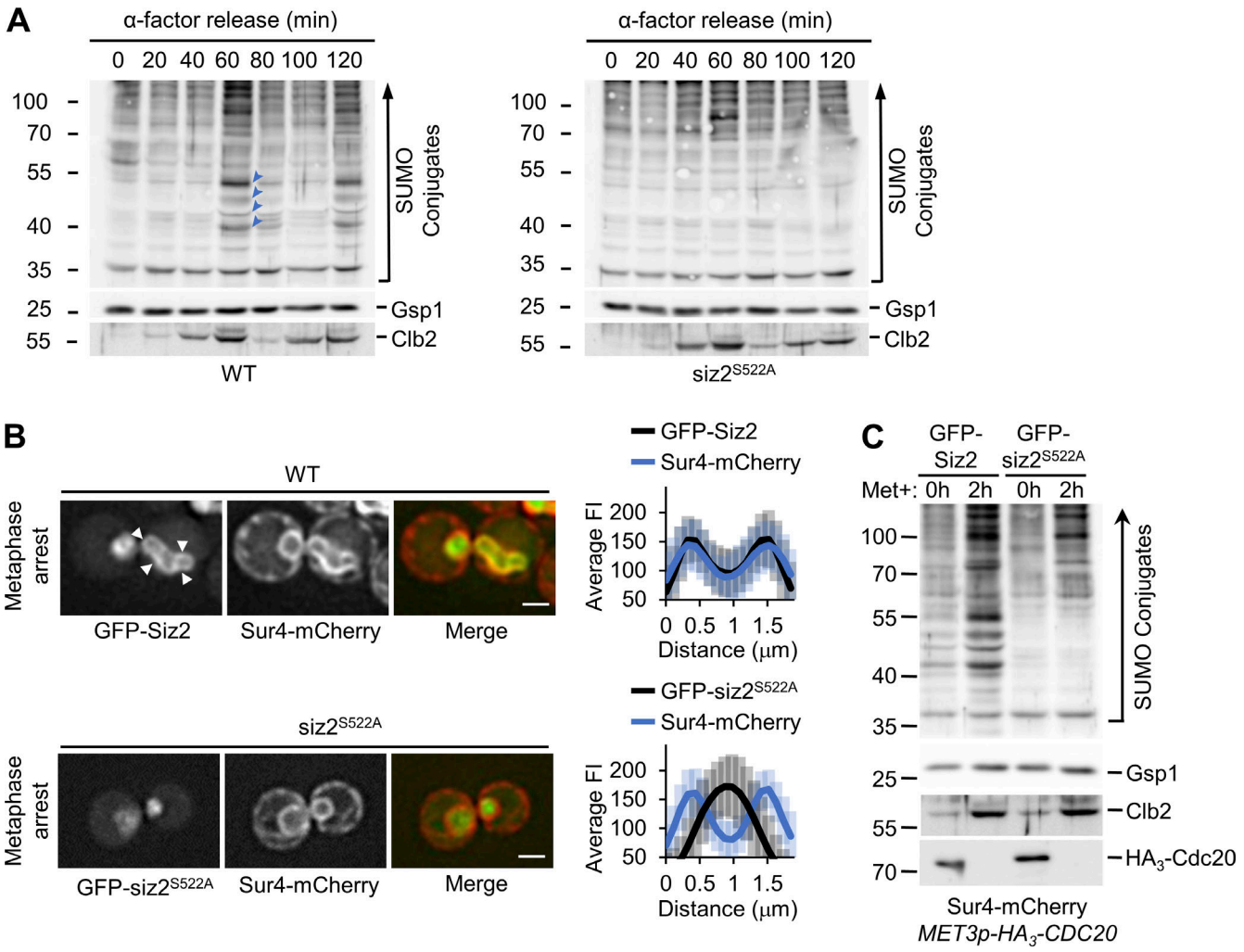

Figure S1. **Siz2 localization and Siz2-mediated SUMOylation events at the NE during mitosis. (A)** WT and siz2S522A cells were arrested in G1-phase (0 min) using α-factor, released from arrest, and then analyzed every 20 min by Western blotting to detect SUMO conjugates, Clb2, and the Gsp1 load control. Clb2 levels peak in metaphase. Arrowheads point to prominent SUMOylated species between 40 and 55 kD in WT cells, which increase in mitosis (peak at 60 min) and decay in G1-phase. **(B)** Representative epifluorescence images are shown for metaphase-arrested MET3pr-HA3-CDC20 cells (2 h after methionine addition) producing either GFP-Siz2 or GFP-siz2^{S522A}. Sur4-mCherry is an NE/ER marker. Arrowheads highlight GFP-Siz2 at the NE. The nuclear distribution of GFP-Siz2 or GFP-siz2^{S522A} relative to Sur4-mCherry was determined using line scan intensities of equatorial optical sections through nuclei. Plots show average fluorescence intensity (FI) for GFP and mCherry at multiple points along a 1.85-μm line for n = 25 nuclei. Size bar, 2 μm. Error bars are SD. **(C)** Cell lysates derived from asynchronous (0) or metaphase-arrested (2 h) cultures of indicated strains were analyzed by Western blotting to assess SUMO conjugate profiles and levels of the indicated proteins. Gsp1 is a loading control. Mass markers are shown in kilodaltons. Source data are available for this figure: SourceData FS1.

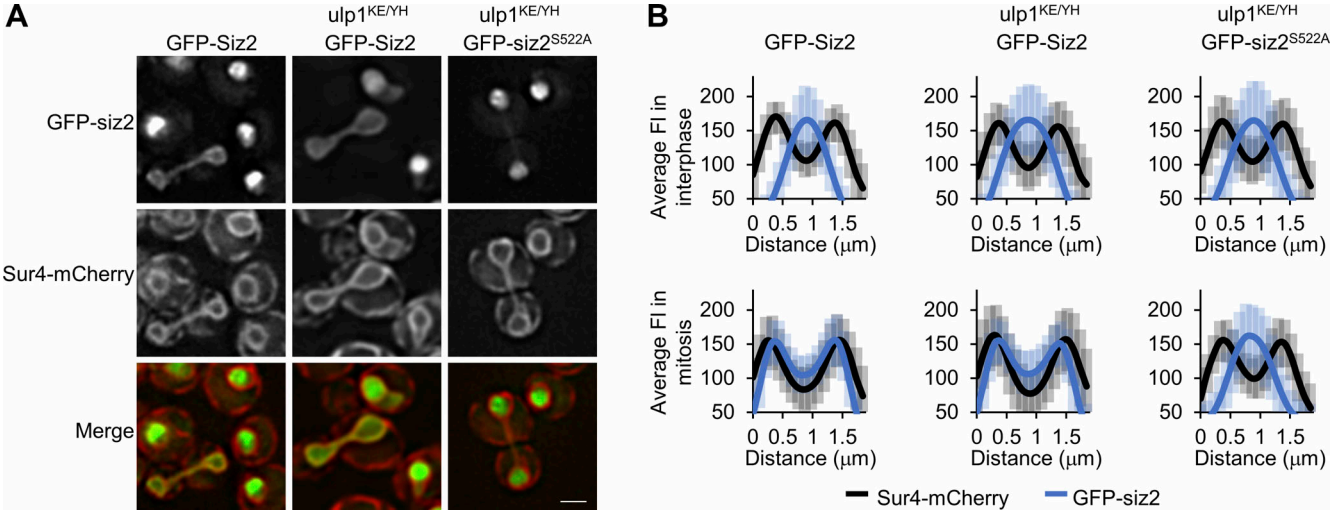

Figure S2. **Siz2 localization to the NE in *ulp1$^{KE/YH}$* mutant cells. (A)** Representative epifluorescence images for the indicated strains producing either GFP-Siz2 or GFP-siz2^{S522A}. Sur4-mCherry is an NE/ER marker. Size bar, 2 µm. **(B)** The nuclear distribution of GFP-Siz2 or GFP-siz2^{S522A} relative to Sur4-mCherry was determined using line scan intensities as described for Fig. S1 B. Error bars are SD.

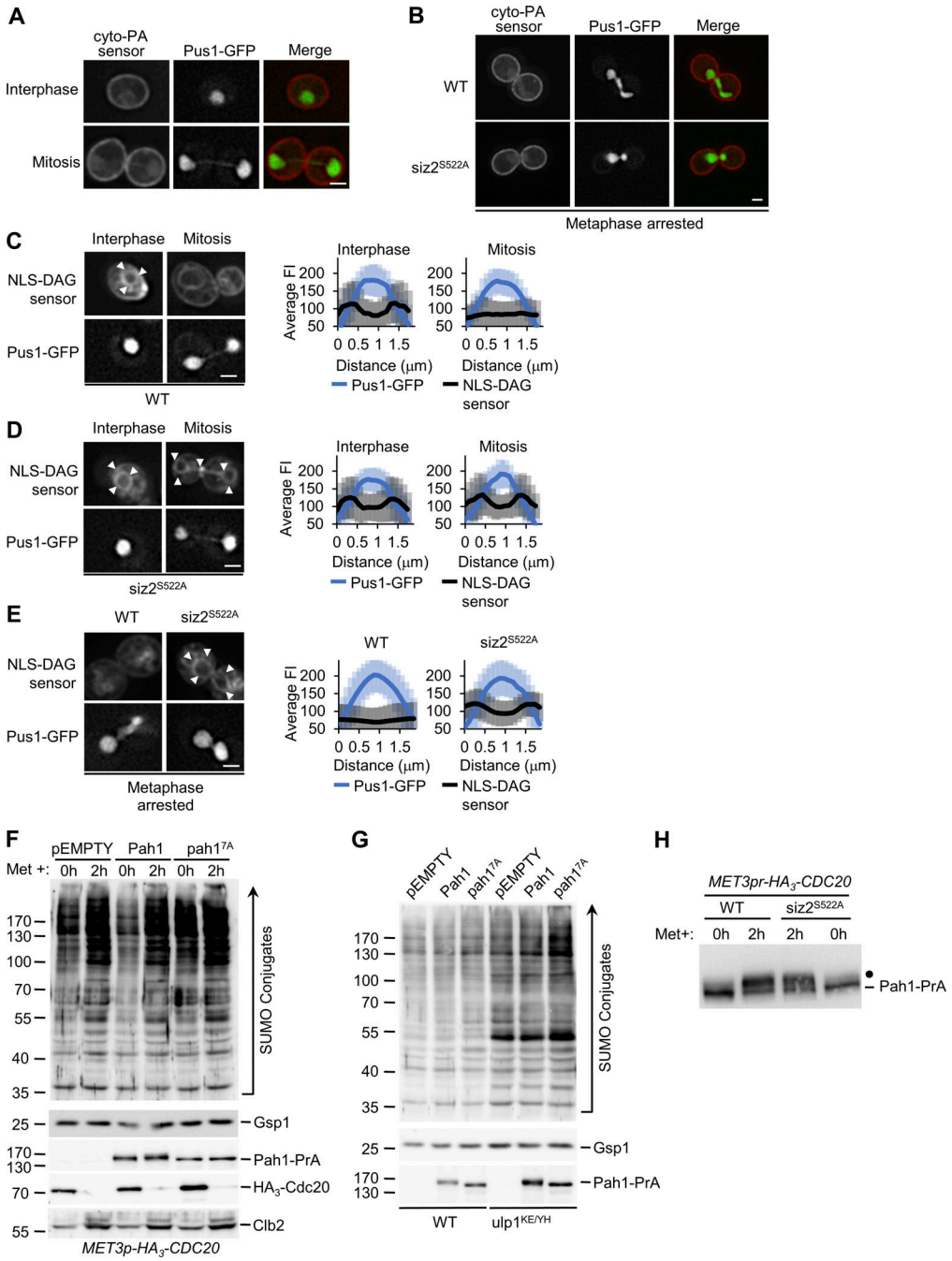

Figure S3. **Cellular distribution of PA and DAG in WT and *siz2*^{S522A} mutant cells. (A)** Asynchronous cultures of WT cells producing Pus1-GFP and the cytoplasmic (cyto)-PA sensor protein (Opi1(Q2)-mCherry; Romanauska and Köhler, 2018) were examined by epifluorescence microscopy. Representative images of interphase and mitotic cells from actively growing cultures are shown. Size bar, 2 µm. **(B)** WT and *siz2*^{S522A} mutant cells containing *MET3pr-HA*$_3$*-CDC20* and producing Pus1-GFP and the cyto-PA sensor were arrested in metaphase, and the distribution of the cyto-PA sensor was examined. Representative images are shown. Size bar, 2 µm. **(C–E)** WT (C) and *siz2*^{S522A} mutant (D) cells producing Pus1-GFP and the NLS-DAG-sensor protein (PKCβ(C1a+C1B)-mCherry; Romanauska and Köhler, 2018) were examined by epifluorescence microscopy. Representative images of interphase and mitotic cells from actively growing cultures are shown. In E, WT and *siz2*^{S522A} mutant cells containing *MET3pr-HA*$_3$*-CDC20* and producing Pus1-GFP and the NLS-DAG-sensor protein were arrested in metaphase by methionine addition. Images show the distribution of the NLS-DAG sensor protein and nuclear Pus1-GFP at 2 h after methionine addition. In C–E, the line scan intensities of the NLS-DAG sensor protein (mCherry) and Pus1-GFP were obtained as described in the Fig. 3 A legend for the indicated strains. Error bars are SD. Arrowheads highlight the NLS-DAG sensor protein along the INM. Size bar, 2 µm. **(F)** Cell lysates derived from asynchronous (0 h) or metaphase-arrested (2 h after methionine addition) cultures of indicated strains were analyzed by Western blotting to assess SUMO conjugate profiles. **(G)** Cell lysates derived from asynchronous cultures of the indicated strains were assessed by Western blotting using an anti-SUMO antibody to visualize SUMO conjugate profiles. Gsp1 is a loading control. **(H)** Asynchronous (0 h) or metaphase-arrested (2 h) cultures of WT and *siz2*^{S522A} mutant cells containing the *MET3pr-HA*$_3$*-CDC20* cassette and expressing *PAH1-PrA* were prepared as described in the Fig. S1 legend. Cell lysates were analyzed by Western blotting to detect Pah1-PrA. The position of phosphorylated forms of Pah1-PrA is indicated by a dot. Mass markers are shown in kilodaltons. Source data are available for this figure: SourceData FS3.

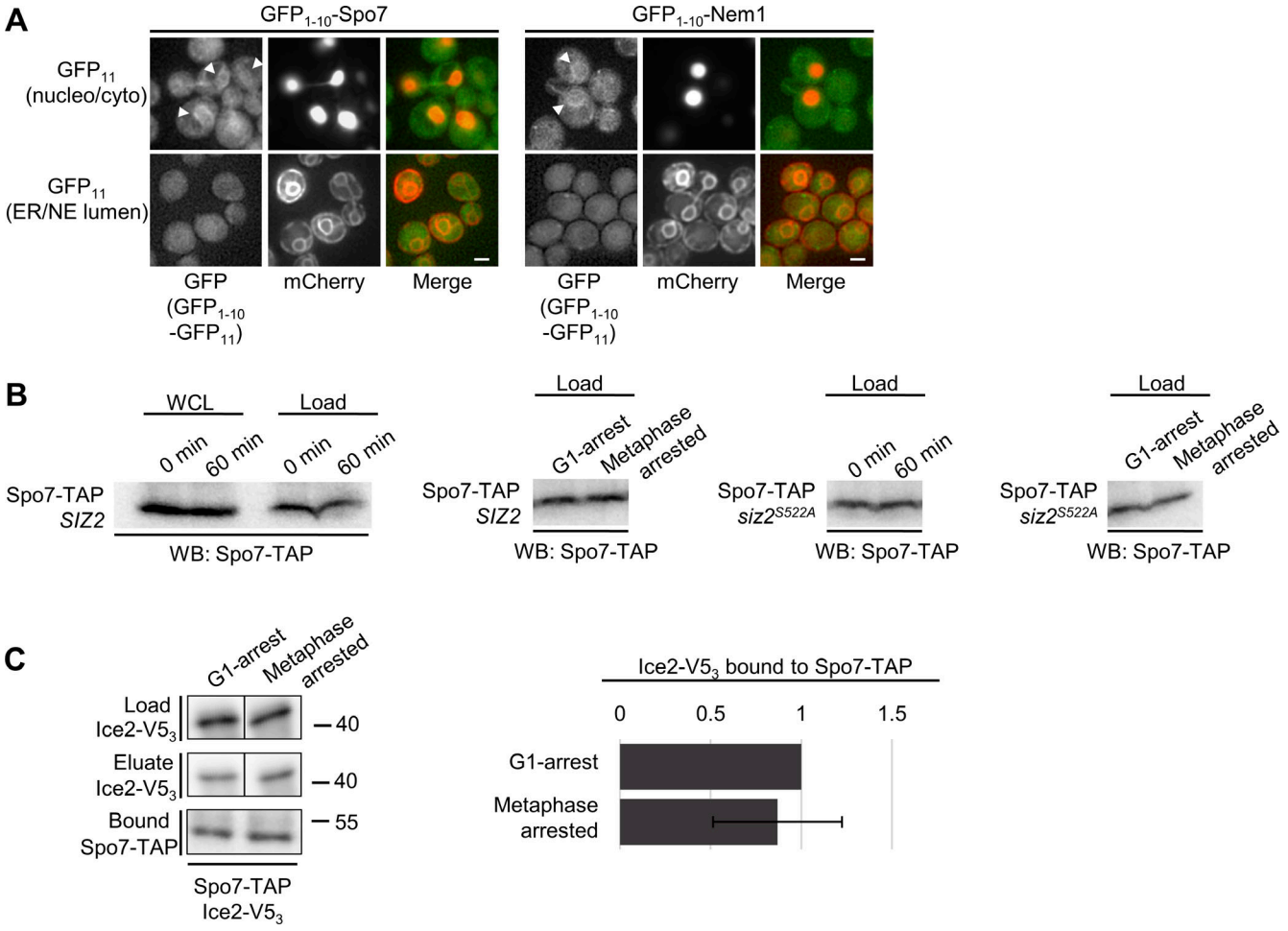

Figure S4. **Localization, levels, and interactions of the Spo7/Nem1 complex. (A)** Spo7 and Nem1 localization was assessed using the split-superfolder GFP system. WT cells producing GFP_{1-10}-Spo7 or GFP_{1-10}-Nem1, as well as plasmid-encoded GFP_{11}-mCherry-Pus1 ($GFP_{11}^{(nucleo)}$) or mCherry-TM-GFP_{11} ($GFP_{11}^{(NE/ER\ lumen)}$), were examined by epifluorescence microscopy. Localization of the GFP_{11} reporter was visualized by mCherry fluorescence. Formation of GFP_{1-10}-GFP_{11} dimers was visualized by GFP fluorescence. Arrowheads point to GFP fluorescence at the NE. Size bar, 2 µm. **(B)** WT cells producing Spo7-TAP (*SPO7-TAP NEM1-V5*$_3$) were arrested with α-factor and then released into the cell cycle for 0 min (G1-phase) and 60 min (mitosis). Whole-cell lysates (WCL) and loads (soluble extracts of WCL used for the affinity-purification of Spo7-TAP) were analyzed by Western blotting (WB) to detect Spo7-TAP. Load fractions are also shown from *SIZ2* and *siz2*^{S522A} cells at the indicated cell cycle stages. In each case, samples compared are derived from equal amounts of total cells. Note, levels of Spo7-TAP in the load fractions are similar in each of the conditions examined. **(C)** Purification and analysis procedures outlined in Fig. 8 were used to analyze Spo7-TAP-bound Ice2-$V5_3$ in WT (*SIZ2*) and *siz2*^{S522A} cells (each containing the *MET3pr-HA*$_3$*-CDC20* cassette) and arrested in G1-phase with α-factor or in metaphase by the depletion of Cdc20 (2 h after methionine addition). Shown are levels of Ice2-$V5_3$ present in the load and elution fractions, and Spo7-TAP bound beads. Note that images shown in each panel were derived from the same Western blot. Black lines indicate that intervening lanes have been spliced out in the top two panels. Adjacent bar graphs in each panel show quantification of the ratio Ice2-$V5_3$ bound (Eluate) to purified Spo7-TAP (Bound) in 3 affinity purification experiments (see Fig. 8 legend and Materials and methods). Mass markers are shown in kilodaltons. Error bars are SD. Source data are available for this figure: SourceData FS4.

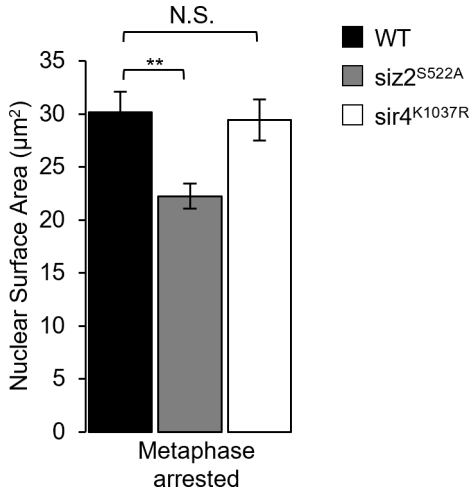

Figure S5. **Nuclear surface area of mutant cells that disrupt chromatin anchoring.** Nuclear surface areas of metaphase-arrested cells from the indicated strains were determined as described in Fig. 1 A. Graphs show data from three biological replicates and 50 cells/replicate/cell cycle stage. Error bars are SD. Asterisks indicate a significant difference relative to WT as determined using a two-tailed Student's *t* test. **p ≤ 0.01. No significant change (N.S.) between WT and the *sir4*^{K1037R} mutant cells was observed.

Provided online are Table S1 and Table S2. Table S1 shows a list of strains and genotypes. Table S2 lists oligonucleotides and sequences.